Journal of Environmental Management 358 (2024) 120682

Contents lists available at ScienceDirect

Journal of Environmental Management

journal homepage: www.elsevier.com/locate/jenvman

Research article

Spatial mapping of land susceptibility to dust emissions using optimization of attentive Interpretable Tabular Learning (TabNet) model

Seyed Vahid Razavi-Termeh [a], Abolghasem Sadeghi-Niaraki [a,*], Armin Sorooshian [b], Tamer Abuhmed [c], Soo-Mi Choi [a]

[a] Dept. of Computer Science & Engineering and Convergence Engineering for Intelligent Drone, XR Research Center, Sejong University, Seoul, Republic of Korea
[b] Department of Chemical and Environmental Engineering, University of Arizona, Tucson, AZ, USA
[c] College of Computing and Informatics, Sungkyunkwan University, Suwon, 16419, Republic of Korea

ARTICLE INFO

Handling Editor: Jason Michael Evans

Keywords:
Dust concentration
Remote sensing
Spatial prediction
Metahurestic algorithms
TabNet model

ABSTRACT

Dust pollution poses significant risks to human health, air quality, and food safety, necessitating the identification of dust occurrence and the development of dust susceptibility maps (DSMs) to mitigate its effects. This research aims to detect dust occurrence using satellite images and prepare a DSM for Bushehr province, Iran, by enhancing the attentive interpretable tabular learning (TabNet) model through three swarm-based metaheuristic algorithms: particle swarm optimization (PSO), grey wolf optimizer (GWO), and hunger games search (HGS). A spatial database incorporating dust occurrence areas was created using Moderate Resolution Imaging Spectroradiometer (MODIS) images from 2002 to 2022, including 15 influential criteria related to climate, soil, topography, and land cover. Four models were employed for modeling and DSM generation: TabNet, TabNet-PSO, TabNet-GWO, and TabNet-HGS. Evaluation of the modeling results using performance metrics indicated that the TabNet-HGS model outperformed the other models in both training (mean absolute error (MAE) = 0.055, root-mean-square error (RMSE) = 0.1, coefficient of determination (R^2) = 0.959), and testing (MAE = 0.063, RMSE = 0.114, R^2 = 0.947) data. Following TabNet-HGS, the TabNet-PSO, TabNet-GWO, and TabNet models demonstrated progressively lower accuracy. The validation of the DSM was performed by assessing receiver operating characteristic (ROC) curves, revealing that the TabNet-HGS, TabNet-PSO, TabNet-GWO, and TabNet models exhibited the highest modeling accuracy, with corresponding area under the curve (AUC) values of 0.994, 0.986, 0.98, and 0.832, respectively. These results highlight the enhanced accuracy of dust susceptibility modeling achieved by integrating swarm-based metaheuristic algorithms with the TabNet model. The dust susceptibility map provides valuable insights into the sources, pathways, and impacts of dust particles on the environment and human health in the study area.

1. Introduction

Airborne dust is a significant environmental problem that affects public health and safety, agricultural productivity, and global climate (Tong et al., 2021). Dust events affect many regions and countries worldwide, including Asia (Cao et al., 2015a,b). In Asia, several countries are exposed to dust events due to their geographical location, climate, and land use practices. The primary sources of dust in Asia are the deserts and arid regions of China, Mongolia, Kazakhstan, Iran, Iraq, Saudi Arabia, and Syria, which generate large amounts of dust particles that can be transported across national and regional boundaries (Yang et al., 2015; Broomandi et al., 2021). The dust events in Asia have increased in frequency and severity in recent years, causing significant environmental, social, and economic impacts, such as air pollution, water scarcity, crop failure, and infrastructure damage (An et al., 2018; Rashki et al., 2018). In Iran, dust events are a major environmental and health issue, especially in the southwest regions, such as the Khuzestan, Bushehr, and Hormozgan provinces (Darvishi Boloorani et al., 2023). As per the Iranian Department of Environment, there has been a documented increase of over 50% in the frequency and duration of dust events in recent decades. These events have had a profound impact, affecting millions of individuals and resulting in substantial economic

* Corresponding author.
E-mail addresses: razavi@sejong.ac.kr (S.V. Razavi-Termeh), a.sadeghi@sejong.ac.kr (A. Sadeghi-Niaraki), armin@arizona.edu (A. Sorooshian), tamer@skku.edu (T. Abuhmed), smchoi@sejong.ac.kr (S.-M. Choi).

https://doi.org/10.1016/j.jenvman.2024.120682
Received 21 July 2023; Received in revised form 13 March 2024; Accepted 14 March 2024
Available online 25 April 2024

losses (Rashki et al., 2021). In Iran, the primary origins of dust can be attributed to the deserts and drylands in the country's central and southeastern regions. These areas are particularly susceptible to wind erosion, drought, and land degradation, making them significant sources of dust particles (Zeinali and Asghari, 2016). According to reports and studies, the Bushehr province of Iran is significantly affected by dust events. Natural and anthropogenic factors, such as desertification, drought, wind erosion, land use changes, and industrial activities, mainly cause dust emissions in these regions (Rahi et al., 2022).

Dust particles can cause respiratory and cardiovascular diseases, reduce visibility and air quality, and damage infrastructure and agriculture (Manisalidis et al., 2020). The impact of dust exposure on human health can vary, encompassing a range of adverse effects. These effects are influenced by factors such as the particles' size, composition, and concentration, as well as the duration and frequency of exposure (Khan and Strand, 2018). Moreover, dust particles can exacerbate existing health conditions, such as allergies, hay fever, and sinusitis, and can cause eye irritation, skin rashes, and other allergic reactions (Kellogg and Griffin, 2006). Various measures can be taken to protect public health from the adverse effects of dust exposure, such as reducing the sources of dust emissions, improving air quality and ventilation, wearing personal protective equipment, and avoiding outdoor activities during dust events. Additionally, early warning systems and public awareness campaigns can inform the public about dust exposure risks and guide how to mitigate the impacts (Tam et al., 2012; Goudarzi et al., 2017).

Traditional dust detection methods, such as ground-based sensors, are often limited in their spatial and temporal coverage and resolution and may not capture the full extent and variability of dust emission and deposition (Von Holdt et al., 2019). Ground-based sensors require costly and time-consuming maintenance and calibration and may be affected by local factors such as terrain, vegetation, and human activities (Allen et al., 2015). Furthermore, ground-based sensors may be unable to detect the sources and pathways of dust located beyond their range, such as in remote or inaccessible areas (Jiao et al., 2021; Abdalla and Peng, 2021). Satellite remote sensing offers a valuable tool for large-scale and continuous dust monitoring, providing spatially explicit and temporally resolved data on dust concentration, distribution, and dynamics (Ayanu et al., 2012; Sowden et al., 2018; Baddock et al., 2021).

Detection and mapping of dust emissions and deposition is essential for identifying sources and sinks of dust, predicting its transport and impact, and developing mitigation and adaptation strategies (Jiao et al., 2021; Boloorani et al., 2021). Dust susceptibility mapping (DSM) has several advantages for environmental management and risk assessment (Jafari et al., 2022). By identifying the areas with a high potential for dust emission and deposition, susceptibility maps can help prioritize monitoring and mitigation efforts, allocate resources and funds effectively, and inform land-use planning and zoning (Gholami et al., 2020a, b,c). Geographic Information Systems (GIS) have several advantages for DSM, as they can integrate and analyze various spatial and non-spatial data sources and generate comprehensive and interactive maps and models (Boroughani et al., 2020). GIS can provide a spatially explicit and temporally dynamic representation of the environmental and anthropogenic factors influencing dust emission and deposition, such as topography, land cover, soil type, climate, human activities, and infrastructure (Jin et al., 2019).

Until now, GIS-based dust susceptibility modeling has predominantly relied on machine learning approaches. For DSM, machine learning and deep learning have several advantages, as they can handle large and complex datasets, extract relevant features, and generate accurate and interpretable models (Murdoch et al., 2019; Jafari et al., 2022). By training on historical and real-time data, machine learning algorithms can capture the spatiotemporal variability of the environmental and anthropogenic factors that affect dust emission and deposition and learn the nonlinear and high-dimensional relationships between them (Balogun et al., 2021).

Boroughani et al. (2020) conducted a DSM study in Khorasan Razavi Province, located in north-eastern Iran. They identified dust centers utilizing Moderate Resolution Imaging Spectroradiometer (MODIS) images from 2005 to 2016. To create their model, they employed two statistical methods: weights of evidence (WOE), frequency ratio (FR), and the random forest (RF) machine learning method. The results indicated accuracies of 82%, 82%, and 91% for FR, WOE, and RF methods, respectively. In a study concerning the prediction of land susceptibility to dust emissions in the Jazmurian Basin, Iran, Gholami et al. (2020a) utilized six machine-learning algorithms: extreme gradient boosting (XGBoost), cubist, bagged multivariate adaptive regression spline (BMARS), adaptive neuro-fuzzy inference systems (ANFIS), Cforest, and Elasticnet. The results indicated a higher accuracy of the Cforest algorithm over the others. Another study by Gholami et al. (2020b) involved spatial mapping of the provenance of storm dust in Khuzestan province of Iran, utilizing several data mining algorithms, including RF, support vector machine (SVM), Bayesian additive regression trees (BART), radial basis function (RBF), XGBoost, regression tree analysis (RTA), Cubist model, and boosted regression trees (BRT), as well as an ensemble modeling (EM) approach. The results highlighted the superior accuracy of EM and XGBoost. Furthermore, Gholami et al. (2021) investigated mapping land susceptibility to atmospheric dust emissions in Iran, employing recurrent neural network (RNN) and restricted Boltzmann machine (RBM) algorithms. The study demonstrated a higher accuracy of RNN compared to RBM. In a study by Jafari et al. (2022), dust spatial modeling was performed using various algorithms, including generalized linear model (GLM), classification tree analysis (CTA), artificial neural network (ANN), MARS, and RF, as well as Maxent (Maximum Entropy), and ensemble algorithms. The findings demonstrated that RF and ensemble algorithms exhibited the highest accuracy. Additionally, the study revealed that precipitation had the most significant impact on dust occurrences. Pourhashemi et al. (2022) determined dust-prone areas along the Iran-Iraq border utilizing remote sensing and machine learning techniques, including MARS, RF, and logistic regression (LR). The research showed that the RF algorithm achieved a superior accuracy of 92% compared to other algorithms. Choubin et al. (2023) conducted a study mapping salty Aeolian dust-source potential areas using MODIS images and the weighted subspace random forest (WSRF) model algorithms. The study compared these methods with three benchmark models: GLM, BRT, and support vector machine (SVM). The results indicated that WSRF outperformed the benchmark models. These algorithms have shown promising results in predicting dust concentrations, identifying dust events, and discriminating between dust and non-dust pixels.

Moreover, these algorithms are often limited by their assumptions, biases, and hyperparameters, which may lead to overfitting, underfitting, or suboptimal performance (Rouzrokh et al., 2022; Razavi-Termeh et al., 2023). Attentive interpretable tabular learning (TabNet) is a deep neural network that uses a novel attention mechanism to select and weigh the relevant features dynamically, adaptively, and hierarchically (Arik and Pfister, 2021). It stands out from traditional machine learning algorithms due to its unique attention mechanism, which dynamically selects and weighs relevant features. Unlike traditional methods, TabNet uses sequential decision-making and interpretable masks to focus on essential features, enhancing accuracy and interpretability adaptively. Specifically, it starts with an empty set, progressively adds informative features, and employs binary masks to indicate feature relevance, allowing for nuanced pattern recognition. This innovative approach enables TabNet to capture intricate relationships within the data, making it a powerful tool for structured data analysis (Si et al., 2019). Like most machine/deep learning models, TabNet has hyperparameters that must be tuned for optimal performance. Finding the best hyperparameter settings may involve an extensive search, which can be computationally expensive and time-consuming. Incorrect hyperparameter choices can result in suboptimal performance or an increased risk of overfitting (Bernardo et al., 2021; Joseph et al., 2022). Metaheuristic algorithms are flexible and can

handle diverse types of hyperparameters, including continuous, discrete, and categorical variables (Gadekallu et al., 2021). They can efficiently explore the search space of TabNet hyperparameters. For this purpose, in this research, three swarm-based metaheuristic algorithms (particle swarm optimization (PSO), grey wolf optimizer (GWO), and hunger games search (HGS)) were used to optimize the hyperparameters of the TabNet algorithm. Swarm-based metaheuristic algorithms are known for their global search ability, robustness, and diversity, making them suitable for complex and nonlinear optimization problems (Binitha and Sathya, 2012).

This study explores the feasibility of utilizing satellite-based imagery combined with a TabNet model to monitor dust events and create a DSM specifically for Bushehr province (Iran), which is an ideal region owing to its high susceptibility to dust emissions (Darvishi Boloorani et al., 2023). Moreover, this study enhances the performance of the TabNet model by integrating three swarm-based metaheuristic algorithms: PSO, GWO, and HGS. These algorithms optimize the TabNet model parameters and improve its accuracy in predicting dust susceptibility. The innovative aspect of this research lies in integrating satellite imagery, the TabNet model, and swarm-based metaheuristic algorithms for dust monitoring and DSM generation. By combining the spatial information from satellite images with the analytical power of TabNet and the optimization capabilities of swarm-based metaheuristics, this study seeks to achieve more accurate and reliable predictions of dust occurrences and susceptibility.

2. Workflow

The research workflow consisted of five main steps, as illustrated in Fig. 1. In the first step, a spatial database was created by collecting dust occurrence data from MODIS images and gathering 15 criteria that influence dust occurrence. Then, the collected data underwent preprocessing and preparation to ensure its quality. Multicollinearity testing assessed the dependence between the influential criteria and identified any multicollinearity issues that may impact the modeling process. After determining the eligibility of factors based on the multicollinearity test results, the WOE method was employed (Step 3). This method calculated the probability of dust occurrence for each class of the selected influential criteria. The results obtained through the WOE method were utilized as inputs for the subsequent modeling phase. The TabNet model was enhanced in the fourth step using three metaheuristic algorithms: PSO, GWO, and HGS. Four models were developed and employed to generate the DSM for the study area: TabNet, TabNet-PSO, TabNet-GWO, and TabNet-HGS. The performance of the models was evaluated using various evaluation indices, including mean absolute error (MAE), root-mean-square error (RMSE), and coefficient of determination (R^2). The generated susceptibility maps were also assessed using receiver operating characteristic (ROC) curves to validate their accuracy (Uddin et al., 2022, 2023a, 2023b).

3. Material and methods

3.1. Study area

The Bushehr province is positioned in the southwestern region of Iran, with its southern boundary adjoining the Persian Gulf (Fig. 2). The region covers an area of approximately 23,198 km^2 and has a population of around 1.2 million people. The Bushehr province has a warm and humid climate, with hot summers and mild winters, influenced by the proximity to the sea and the surrounding mountains. The province experiences a wide range of temperatures, with the highest recorded temperature reaching 52.5 °C and the lowest dropping to −1 °C. On average, the annual temperature of the province stands at 25.7 °C.

Additionally, the area receives an average rainfall of 217 mm per year. The province has a diverse landscape consisting of coastal plains, mountains, and deserts, characterized by various natural resources and ecosystems. The coastal plains are essential for agriculture, fisheries, and tourism, while the mountains provide water resources, biodiversity, and scenic views. The deserts, such as the Dasht-e Kavir and Dasht-e Lut, are among the most significant and driest deserts in Iran and have a considerable impact on the region's climate, geology, and ecology. The Bushehr province has been identified as one of the most affected regions by dust events in Iran due to its location in the path of the prevailing winds from the deserts and drylands in the central and southeastern parts of the country. The dust events in the Bushehr province have increased in frequency and severity in recent years, causing significant environmental, social, and economic impacts, such as air pollution, reduced visibility, crop failure, and infrastructure damage (Hamzeh et al., 2021; Rahi et al., 2022). Fig. 3 represents photos of dust within the study area.

3.2. Dust detection and inventory map

This investigation utilized MODIS Terra and Aqua satellite data to monitor dust patterns. These satellite images were employed to track aerosol optical depth (AOD) over 21 years (2002–2022) using the Google Earth Engine (GEE) system. To achieve this goal, this study employed a combination of the MCD19A2 V6 dataset and the multi-angle implementation of the atmospheric correction (MAIAC) algorithm. This integration enabled them to monitor the level 2 AOD with a high spatial resolution of 1 × 1 km. To enhance the accuracy of cloud detection, aerosol retrievals, and atmospheric correction, a cutting-edge technique called MAIAC was employed, which incorporates time series analysis and a hybrid approach involving pixel- and image-based processing (Muthukumar et al., 2022). The aerosol concentration was determined using the blue band of MODIS images over 21 years. The temporal pattern of dust occurrence between 2002 and 2021 is shown in Fig. 4. The regions identified as high-risk were transformed into 519 data locations for modeling, with 70% (363 locations) assigned for training and 30% (156 locations) for validation (Fig. 5).

3.3. Effective criteria

For identifying dust-effective factors in this research, we selected 15 influential criteria for the occurrence of dust. These criteria were based on previous studies (Boroughani et al., 2020; Gholami et al., 2020a,b,c; Jafari et al., 2022; Pourhashemi et al., 2022) and expert opinions. The selected criteria were classified into four categories: topography (altitude, aspect, and slope), climate (rainfall and wind speed), soil properties (bulk density, sand, clay, soil water content, soil texture, and soil order), and land properties (land cover, lithology, distance to river, and normalized difference vegetation index (NDVI)) (Table 1). Each criterion is explained in Fig. 6a-o. We used ArcGIS 10.8 software and the GEE platform to process and prepare the data.

The topography criteria (altitude, aspect, and slope) were obtained from the digital elevation model (DEM) extracted from the shuttle radar topography mission (SRTM) images. The pixel size of these images was 30 × 30 m, and processing was carried out using the GEE platform. For the climate criteria (rainfall and wind speed), 20-year average data from 10 synoptic stations (Fig. S1) in Bushehr province were used to create the corresponding maps. ArcGIS 10.8 software and the inverse distance weighting (IDW) interpolation method were employed for this task, with a 30 × 30 m pixel size.

Regarding soil properties, we considered six criteria: bulk density, sand, clay, soil water content, soil texture, and soil order. Data from the United States Department of Agriculture (USDA) from 2000 to 2018, available in the GEE platform, were utilized to generate these criteria. The soil order map was created using the soil maps of Bushehr province. The pixel size for these criteria was set at 250 × 250 m. For land properties, a land cover map in 2017 was generated by combining Sentinel-1 and Sentinel-2 images within the GEE platform, following the methodology proposed by Ghorbanian et al. (2020). The lithology map

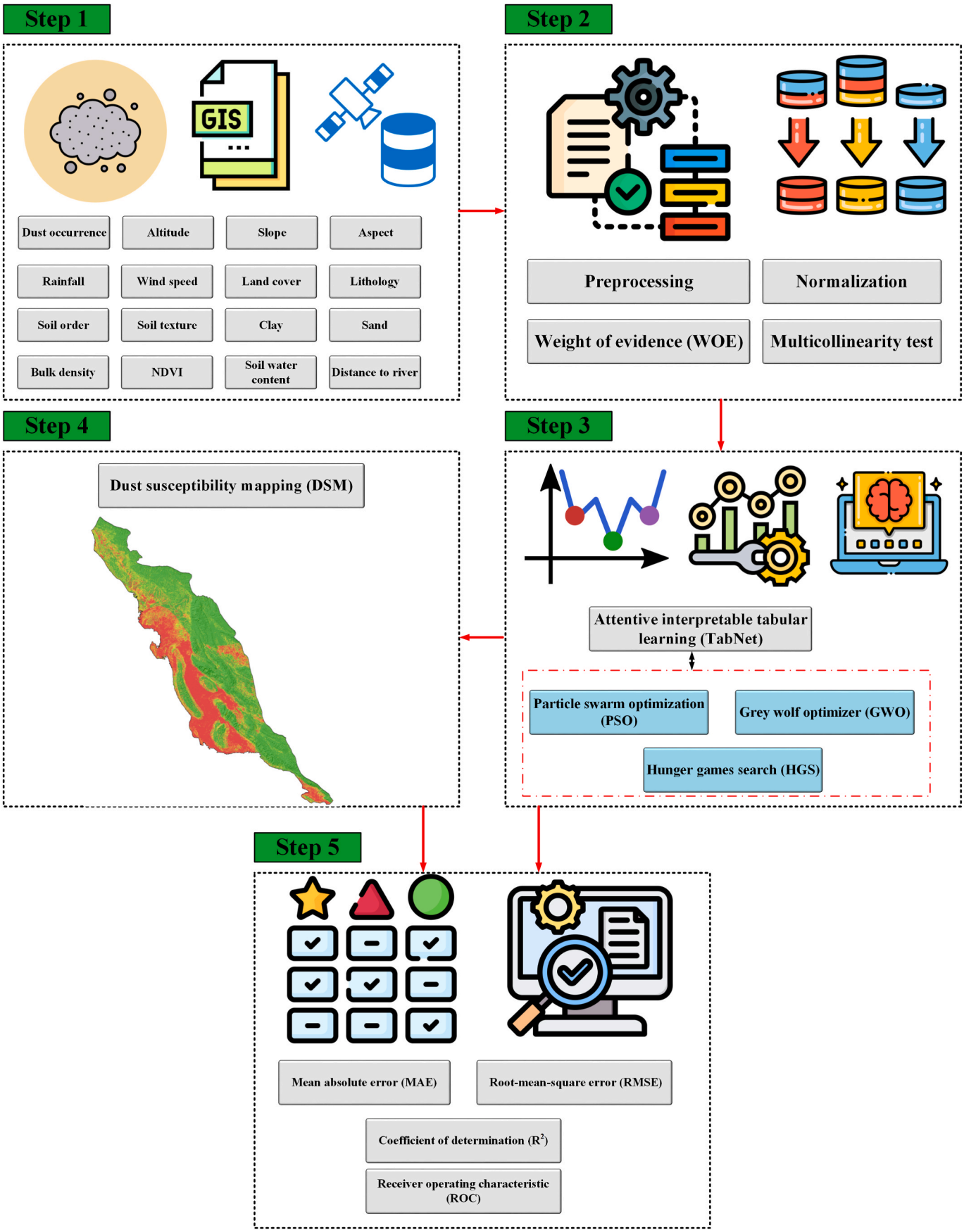

Fig. 1. A visual guide to the research workflow.

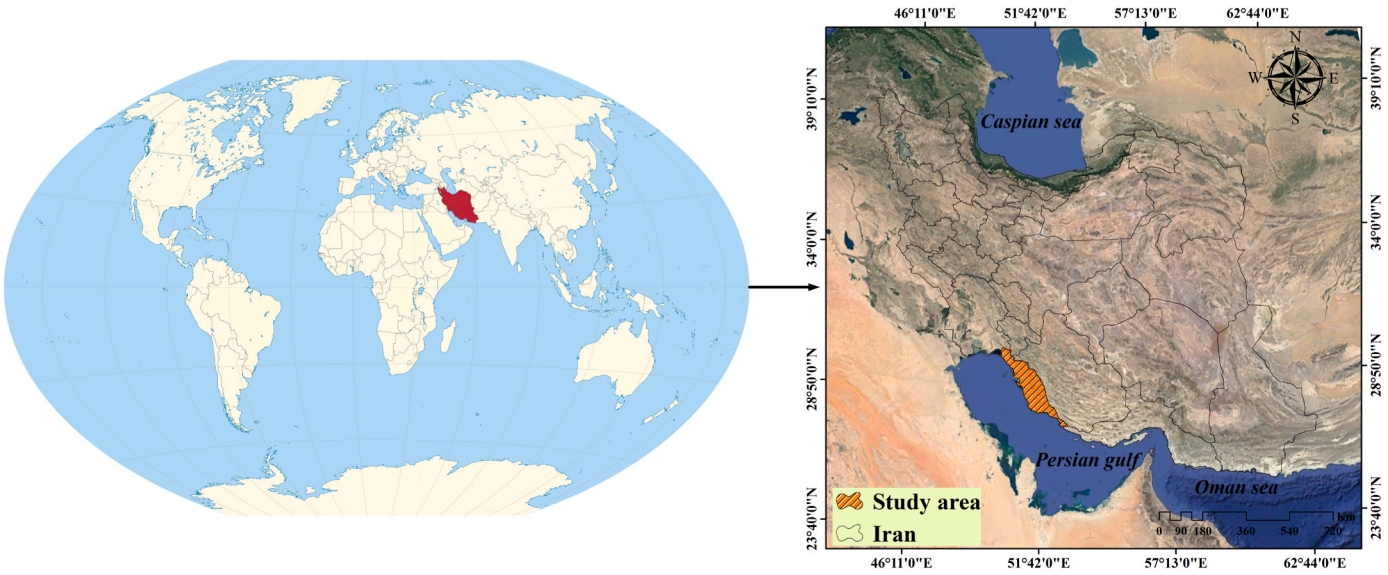

Fig. 2. Geographic overview of the study area.

Fig. 3. Photos of dust occurrence in the study area.

was created using data from the Iran geological maps at a scale of 1:100, 000. The NDVI criterion, which is indicative of vegetation cover changes, was calculated using Landsat-8 images (2013–2022) in the GEE platform, following the Equation:

$$\mathrm{NDVI} = (\mathrm{Band\ 5} - \mathrm{Band\ 4}) / (\mathrm{Band\ 5} + \mathrm{Band\ 4}) \quad (1)$$

where "Band 4" corresponds to the red spectral band of the Landsat-8 Operational Land Imager (OLI) sensor, while "Band 5" represents the near-infrared spectral band. We utilized the DEM to obtain the river layer, which was then rasterized using the Euclidean distance method. For modeling, the pixel size of all criteria was converted to 250 × 250 m. Resampling techniques were used to equalize the pixel sizes of the

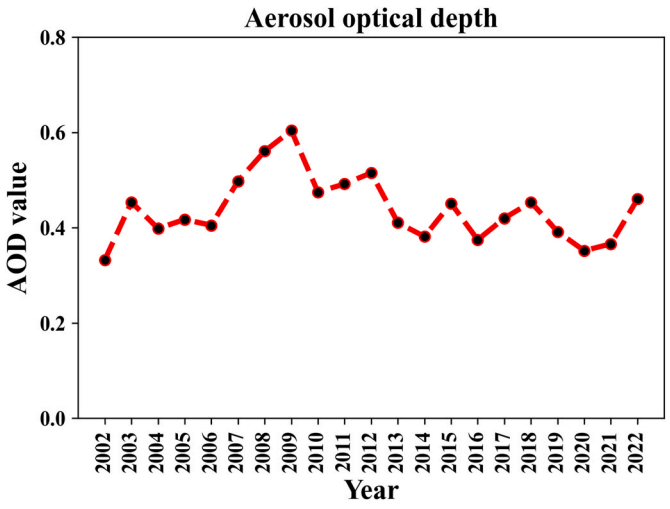

Fig. 4. Temporal patterns of dust occurrence in the study area.

criteria. For this purpose, the nearest method was used for discrete data, and the bilinear method was used for continuous data.

3.4. Multicollinearity test

Multicollinearity refers to a statistical concept utilized in regression analysis to describe a situation where two or more independent variables display a significant level of correlation (Farahani et al., 2022). This correlation can be moderate to high, leading to inaccurate or misleading analytical results. Various techniques exist for measuring multicollinearity, and one widely employed approach in earth science applications is the use of variance inflation factors (VIF) and tolerances (Franke, 2010; Mehravar et al., 2023). The categorization of VIF values indicates the absence of correlation when VIF equals 1, moderate multicollinearity when the value falls between 1 and 5, medium multicollinearity when VIF equals 5, and high multicollinearity when the value ranges between 5 and 10 (Parween et al., 2022). In regression analysis, a general guideline suggests that if the VIF exceeds 10 for a particular independent variable, it indicates multicollinearity (Shabanpour et al., 2022).

3.5. Weight of evidence (WOE) method

The WOE is a statistical method that utilizes the Bayesian probability framework to statistically evaluate the comparative significance of conditioning factors (Lee et al., 2018). This approach determines the prior probability by analyzing historical data on dust occurrences. The WOE method calculates the weights for each dust conditioning factor (F) as positive (W^+) and negative (W^-) based on the presence or absence of dust sites (D) (Equations (2) and (3)) (Razavi-Termeh et al., 2021).

$$W^+ = \ln\left(\frac{p\{D|F\}}{p\{D|\overline{F}\}}\right) \quad (2)$$

$$W^- = \ln\left(\frac{p\{\overline{D}|F\}}{p\{\overline{D}|\overline{F}\}}\right) \quad (3)$$

P is the symbol for probability, D indicates the presence of dust conditioning factors, whereas $\overline{D}$ signifies their absence. F denotes the presence of dust, while $\overline{F}$ shows the absence of dust. A weight with a positive value signifies the existence of a dust conditioning factor at specific dust sites, indicating a direct association with the presence of dust. On the contrary, a weight with a negative value implies the lack of a dust conditioning factor and signifies a negative relationship between its absence and the occurrence of dust (Batar and Watanabe, 2021). Next, a weighted contrast factor (C) is calculated to assess the spatial association between the conditioning factor and dust. C displays a negative value to indicate a negative spatial relationship, while C exhibits a positive value to signify a positive relationship. Equations (4) and (5) are employed to calculate the values of C and its corresponding standard deviation S(C) for W (Tehrany et al., 2014).

$$C = W^+ - W^- \quad (4)$$

$$S(C) = \sqrt{S^2(W^+) + S^2(W^-)} \quad (5)$$

The variance of W^+ is denoted as $S^2(W^+)$, while the variance of W^- is represented as $S^2(W^-)$. The calculation of the final weight (W) for each

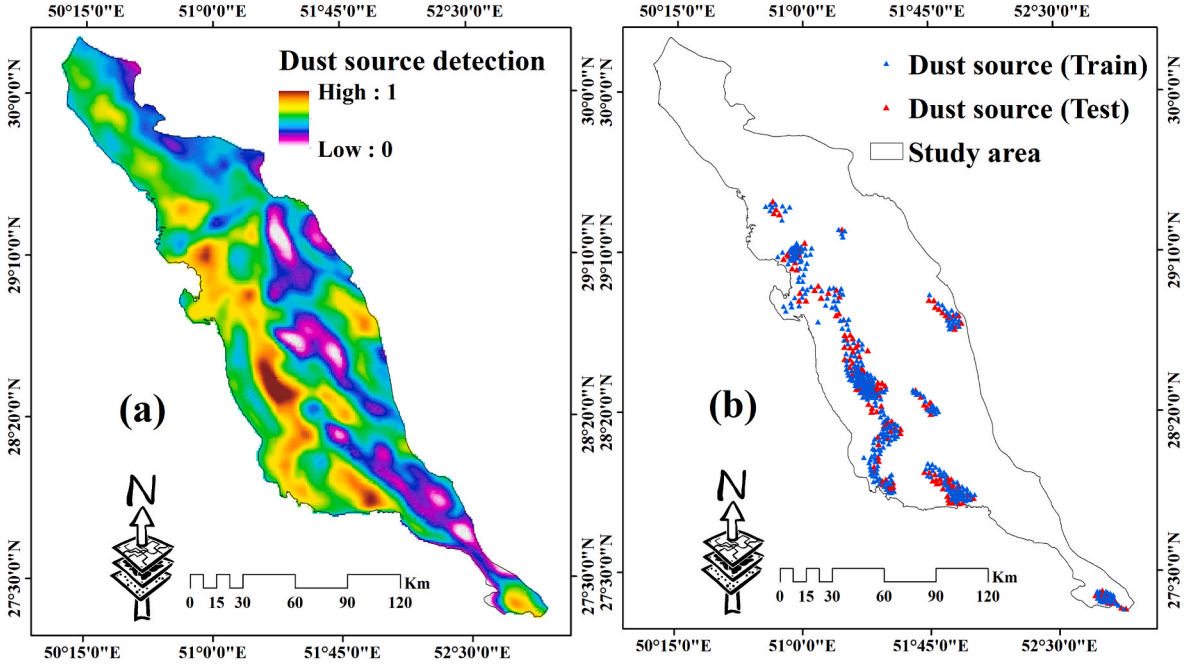

Fig. 5. Dust map in study area: a) Dust source detection, and b) Dust inventory map.

Table 1
Information about the factors influencing dust.

Factors	Data source	Type	Scale/ Resolution
Rainfall	Iranian Meteorological Organization (IMO)	Sheet	30 m
Wind speed	Iranian Meteorological Organization (IMO)	Sheet	30 m
Digital elevation model (DEM)	Shuttle radar topography mission (SRTM) images	Raster	30 m
Altitude	DEM	Raster	30 m
Slope	DEM	Raster	30 m
Aspect	DEM	Raster	30 m
Soil texture	United States Department of Agriculture (USDA)	Raster	250 m
Bulk density	United States Department of Agriculture (USDA)	Raster	250 m
Sand	United States Department of Agriculture (USDA)	Raster	250 m
Clay	United States Department of Agriculture (USDA)	Raster	250 m
Soil water content	United States Department of Agriculture (USDA)	Raster	250 m
Soil order	Iran's Natural Resources and Watershed Management Organization	Vector	1:100,000
Distance from the river	DEM	Vector	1:50,000
Lithology	Geological maps of Iran	Vector	1:100,000
Land cover	Sentinel-1 and Sentinel-2 images	Raster	30 m
Normalized difference vegetation index (NDVI)	Landsat-8 satellite imagery	Raster	30 m

class of factors influencing dust is determined using Equation (6) (Razavi-Termeh et al., 2021).

$$W = \frac{C}{S(C)} \tag{6}$$

3.6. Attentive Interpretable Tabular Learning (TabNet) model

TabNet operates on a tree-like structure and facilitates the combination of features by assigning coefficients to determine their influence in the decision-making procedure (Shah et al., 2022). TabNet utilizes sparse instance-wise feature selection to acquire knowledge from a training dataset. Additionally, it constructs a sequential multi-step architecture that identifies decision components at each step by using the selected features (McDonnell et al., 2023). At each nth step, TabNet processes a feature vector of D dimensions, and the output of each stage is directed to a feature transformer block. Several universal or stage-specific layers make up the feature transformer building block. Fully-connected layers, a batch normalization layer, and an activation function based on gated linear units (GLUs) comprise these layers (Arik and Pfister, 2021). In addition, the residual normalization connection implemented in the GLU aids in keeping the network's variance constant. By employing this multi-layered block, the network gains the ability to select relevant features effectively and achieve improved parameter efficiency. The feature transformer is linked to the attentive transformer and mask to provide a reliable feature selection at each stage. This integration guarantees a dependable and resilient feature selection process throughout the analysis, enhancing the system's overall reliability (Yan et al., 2021). The attentive transformer is formulated in Equation (7), a multi-layer block that includes completely connected and batch normalization layers. The masking technique and the attentive transformer are crucial in the overall methodology (McDonnell et al., 2023).

$$a[i-1] : M[i] = \text{sparsemax}(P[i-1].h_i([a-1])) \tag{7}$$

In Equation (7), the variables " $a[i-1]$" represent the previous step, " $P[i]$" represents the priori scale, and " h_i" represents a trainable function. The sparsemax activation function and the prior are integral parts of the immersed transformer. The dimensionality of feature vectors is lowered by the sparsemax activation function's introduction of sparsity. To do this, it maps the features onto a probability space in Euclidean space, which improves the data's representation and interpretation (Asencios et al., 2023). The introduction of the sparsemax activation function enables each projected feature vector to be associated with a probability, thereby enhancing the interpretability of the model. Furthermore, the relevance or salience of a feature across the earlier phases is indicated by the last scale word, "P[i]". Its calculation is defined by Equation (8), providing a quantitative measure of the feature's significance throughout the analysis (McDonnell et al., 2023).

$$P[i] = \prod_{j=1}^{i} (\gamma - M[j]) \tag{8}$$

The "γ" variable specifies the connection between the number of decision steps required to enforce a feature and the number of decision steps taken. The feature is only enforced at the given decision step when the value of "γ" is 0. When "γ" is set to 1, it indicates that the feature is enforced at the provided action and across many stages (McDonnell et al., 2023). The primary function of the attentive transformer is to identify and select the most salient features, which are then utilized to construct the transformed feature vector. This vector is subsequently passed through the learnable Mask, denoted as " M[j]". The mask's utility extends beyond merely improving interpretability to fine-tune the feature selection process begun by the watchful transformer. A coefficient is constructed that gives each procedure stage its proper due by aggregating the masks at each one (McDonnell et al., 2023).

3.7. Swarm-based metahurestic algorithms

3.7.1. Hyperparameters tuning

To optimize the TabNet model, this study employed three swarm-based algorithms: PSO, GWO, and HGS. The primary aim was to optimize seven hyperparameters of the TabNet model using these algorithms. These hyperparameters included n_d (dimension of the prediction layer), n_a (dimension of the attention layer), n_steps (number of successive steps in the network), n_independent (number of independent GLU layers), n_shared (number of shared GLU layers), gamma, and momentum. The objective was to find the best combination of hyperparameters for the TabNet model using these metaheuristic algorithms through multiple iterations while minimizing the RMSE index (Equation (9)). The RMSE index serves as an objective function, with lower values indicating greater convergence of the metaheuristic algorithms.

$$RMSE = \sqrt{\frac{1}{N}\sum_{i=1}^{N}(y_i' - y_i)^2} \tag{9}$$

In Equation (9), N represents the number of data points, y_i' represents the predicted value for the ith data point, and y_i represents the actual value for the ith data point. In the subsequent sections, each of these algorithms will be comprehensively explained. The flowchart of the hybrid TabNet models is shown in Fig. 7. The first step in this process involves the initialization of the algorithm. Once the initialization is complete, the next step is the fitness evaluation. In this step, each particle in the PSO, each wolf in the GWO, and each hunger in the HGS population has its fitness evaluated. Fitness is calculated based on the performance of the TabNet model using a predefined metric, such as the RMSE. Lower RMSE values indicate better fitness, signifying a closer match between the model predictions and the actual data. Following fitness evaluation, the algorithms proceed to update their solutions. In PSO, personal best positions for each particle and the global best position are updated based on fitness values. In GWO, alpha, beta, and delta wolves, representing

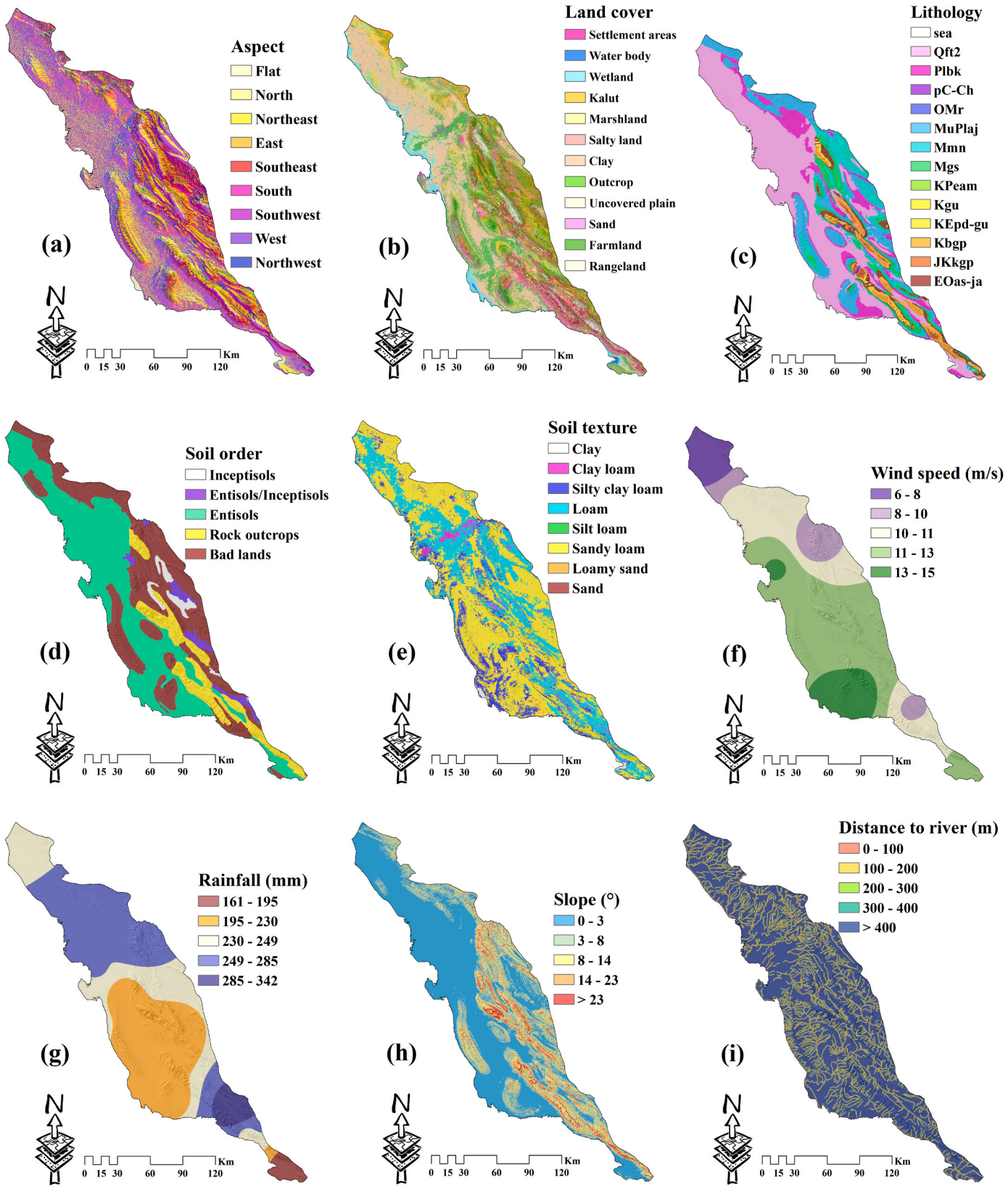

Fig. 6. Factors influencing dust: a) Aspect, b) Land cover, c) Lithology, d) Soil order, e) Soil texture, f) Wind speed, g) Rainfall, h) Slope, i) Distance to river, j) NDVI, k) Altitude, l) Bulk density, m) Sand, n) Clay, and o) Soil water content.

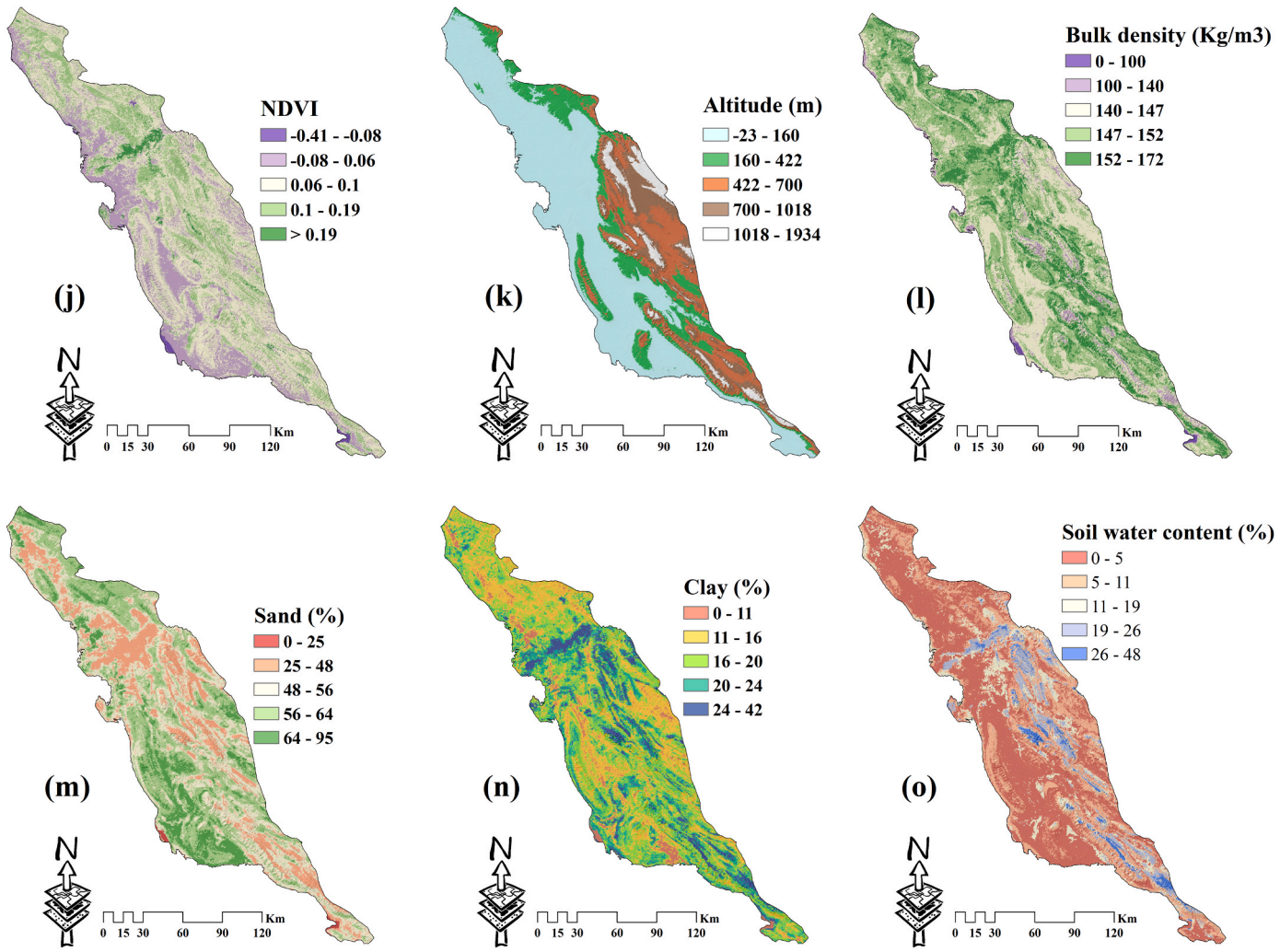

Fig. 6. (*continued*).

the best solutions, are determined, and other wolves adjust their positions based on these leaders. In HGS, the individual is updated, considering the best solutions found so far. The iterative process continues until a stopping criterion is met. Common criteria include reaching a maximum number of iterations or achieving a specific convergence tolerance. Once the stopping criterion is satisfied, the best hyperparameter set is extracted based on the optimal position in the final population. Finally, with the optimized hyperparameters in hand, the TabNet model is trained. These hyperparameters represent the configuration that resulted from the meta-heuristic algorithms' search process, aiming to fine-tune the model for optimal performance.

3.7.2. *Particle Swarm Optimization (PSO) algorithm*

The PSO algorithm is a population-based stochastic optimization technique that draws inspiration from the collective behavior observed in bird flocking or fish schooling (Kulkarni et al., 2015). In PSO, a group of particles represents potential solutions within the search space of a given problem. Each particle modifies its position based on the best places it has previously known and the best positions found collectively by the swarm (Juneja and Nagar, 2016). This adjustment is guided by the particle's velocity, which influences its movement toward promising regions in the search space (Kameyama, 2009). The algorithm involves the following steps (Onwunalu and Durlofsky, 2010; Jain et al., 2022):

- Initialization: A population of particles is initialized, where each particle is assigned random positions and velocities within the search space. The initial positions of the particles are set as their individual best positions.
- Update the velocity and position of the particles: Particle velocities are revised in light of each one's current speed, cognitive part, and social part. The new velocity of a particle is calculated using the following Equation:

$$V(i+1) = w * V(i) + c_1 r_1 (p_{best} - x(i)) + c_2 r_2 (g_{best} - x(i)) \quad (10)$$

Equation (10) calculates the updated velocity of a particle in PSO at the $(i+1)^{th}$ iteration. It incorporates an inertia weight (w), acceleration coefficients (c_1 and c_2), random numbers (r_1 and r_2), the particle's personal best position (p_{best}), the best position of any particle in the swarm (g_{best}), and the current position of the particle (x(i)). The particle's position is then updated based on the new velocity.

- Evaluate and update the particle's best positions: Using the objective function (the RMSE index), we may determine whether or not the current position of each particle is optimal. If the current position's fitness surpasses the particle's previous best-known position, the particle's most prominent position is updated accordingly.
- Update swarm's best position: Each particle's best-known position is evaluated for its fitness. The best location of the swarm is updated if a particle's fitness is higher than the current best position.
- Termination: Steps 2 to 4 are repeated until a termination condition is met. This could mean getting to a certain fitness level or several iterations.

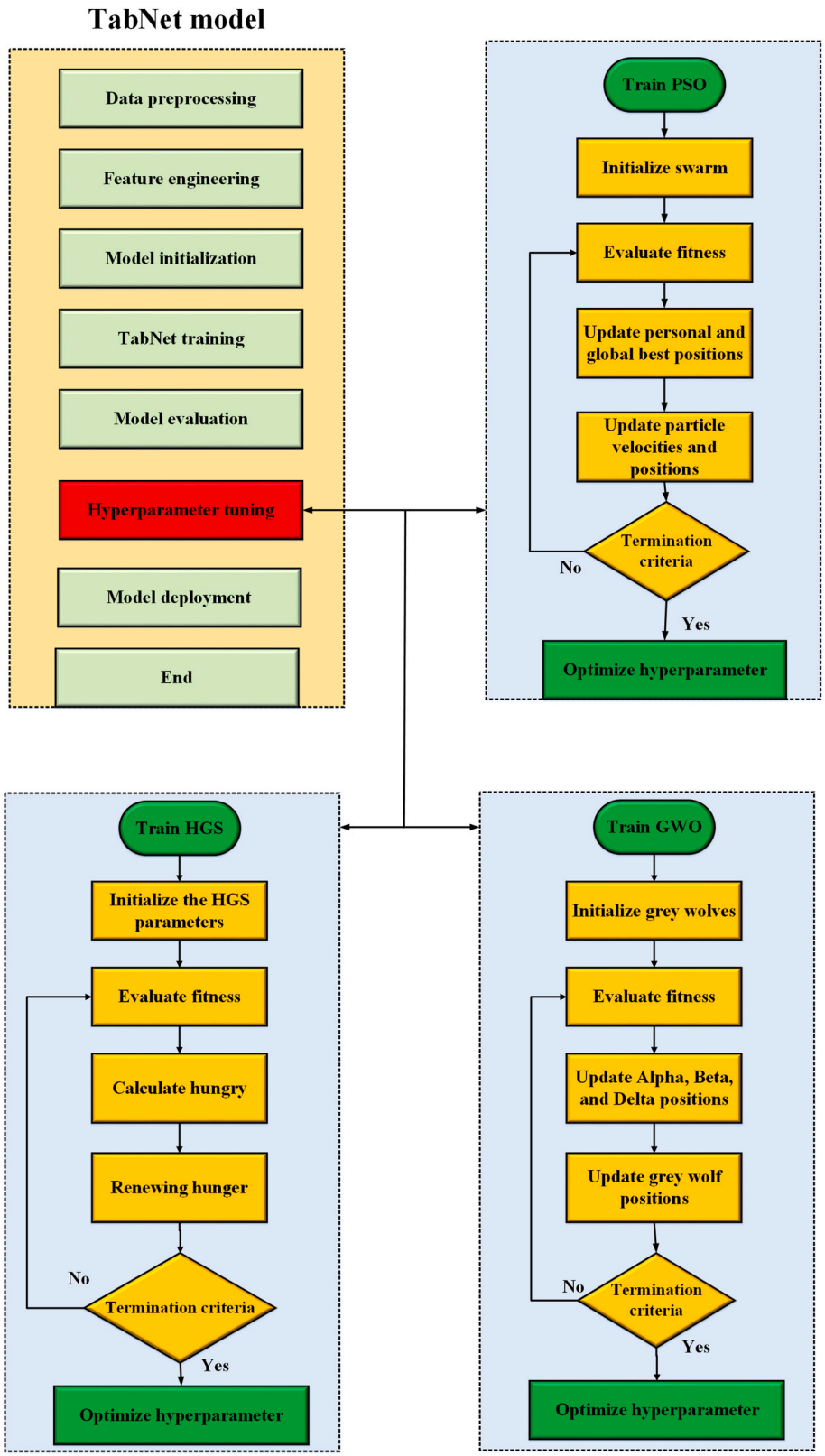

Fig. 7. Flowchart of hybrid TabNet models.

3.7.3. Grey Wolf Optimization (GWO) algorithm

The GWO algorithm is a form of optimization theory conceptualized from observing the natural hierarchy and foraging practices of grey wolves (Li and Luk, 2019). In GWO, the population of candidate solutions is represented by a pack of grey wolves, which imitates the hunting dynamics and cooperation among wolves to find the best solution (Shahin et al., 2023). The algorithm involves the following steps (Tikhamarine et al., 2020; Nadimi-Shahraki et al., 2021):

- Initialization: Initialize a population of grey wolves, where each wolf represents a potential solution within the search space. The initial positions of the wolves are determined randomly.
- Update wolf's position: The wolves' location is constantly being revised about that of the pack's alpha, beta, and delta wolves. The following equation is used to determine where each wolf will be in the future:

$$X(i+1) = X_p(i) - \overrightarrow{A} * \overrightarrow{D} \tag{11}$$

The following location of a wolf is denoted by X(i+1). The position vector of the grey wolf is $X_p(i)$, where i represent the current iteration. The matrix coefficient $\overrightarrow{A}$ is utilized in the algorithm, along with the distance $\overrightarrow{D}$ that separates the grey wolf from the prey. These parameters are calculated using the following Equations:

$$\overrightarrow{D} = \left| \overrightarrow{C} * X_p(i) - X(i) \right| \tag{12}$$

$$\overrightarrow{A} = 2 * a * r_1 - a \tag{13}$$

$$\overrightarrow{C} = 2 * r_2 \tag{14}$$

During the iterations, "a" experiences a linear decrease from 2 to 0, while " r_1" and " r_2" represent random numbers generated within the range of 0–1.Evaluate and update wolf's dominance: The position dominance of each wolf is evaluated based on fitness assessments using the objective function (RMSE index). If a wolf has better fitness than the alpha, beta, or delta wolves, it becomes the new pack leader.

- Termination: Steps 2 and 3 are repeated until a termination condition (e.g., the maximum number of iterations or the desired fitness threshold is reached).

3.7.4. Hunger Games Search (HGS) algorithm

HGS, introduced by Yang et al. (2021), is an innovative population-based optimization algorithm that operates without gradients. It draws inspiration from the cooperative foraging behaviors observed in social animals, where the intensity of these behaviors correlates with the animals' hunger levels (Ma et al., 2022). In HGS, a key aspect is incorporating an adaptive weight that emulates the influence of hunger within the logical rules, or "games," employed in each search step. This adaptive weight introduces a dynamic, straightforward framework that enhances the algorithm's performance. Due to the significant impact hunger has on maintaining homeostatic balance and influencing the decision-making and actions of animals, it is widely recognized as a crucial factor (Fahim et al., 2021). As hunger intensifies, the desire for food increases accordingly.

Furthermore, in the context of the HGS algorithm, "games" refers to the logical rules universally adopted by animals for survival. These rules encompass various behaviors, including searching for food and defending against predators. These games serve as fundamental strategies animals employ to enhance their chances of survival. When food resources are scarce, a logical game unfolds among hungry animals, wherein they compete and strive to secure the available food resources. This competition determines the victor who successfully obtains the little food during that particular instance. The HGS algorithm encompasses several stages: initialization, assessing fitness, arranging in order, updating hunger, updating weight, and updating location (Ma et al., 2022).

- Approaching Food: The location of the individual at a time (t) is determined by its foraging behavior, which can be mathematically represented as follows (Adel et al., 2022):

$$\overrightarrow{X(t+1)} = \begin{cases} \text{Game 1}: \overrightarrow{X(t)} * (1 + \text{rand}(1))\text{m}\, r_1 < l \\ \text{Game 2}: \overrightarrow{W_1} * \overrightarrow{X_b(t)} + \overrightarrow{R} * \overrightarrow{W_2} * \left| \overrightarrow{X_b(t)} - \overrightarrow{X(t)} \right|, r_1 > l, r_2 > E \\ \text{Game 3}: \overrightarrow{W_2} * \overrightarrow{X_b(t)} - \overrightarrow{R} * \overrightarrow{W_2} * \left| \overrightarrow{X_b(t)} - \overrightarrow{X(t)} \right|, r_1 > l, r_2 < E \end{cases} \tag{15}$$

The position of each individual is represented by $\overrightarrow{X(t)}$, while $\overrightarrow{X_b(t)}$ indicates the location of the best individual. The "weight of hunger" is denoted by $\overrightarrow{W_1}$ and $\overrightarrow{W_2}$. (1) is a randomly generated number. r_1 and r_2 are two random numbers within the range of [0,1]. Furthermore, to enhance the algorithm's performance, an additional parameter l is incorporated, while E is utilized as a control for variations. In this section, the instructions for the population are categorized into two aspects: $\overrightarrow{X}$-based and $\overrightarrow{X_b}$-based. The initial game emphasizes independent hunting behavior, without collaboration or teamwork, for a few individuals. The final two games replicate the cooperative gathering actions involving $\overrightarrow{R}$, $\overrightarrow{W_1}$, and $\overrightarrow{W_2}$. These different regulations offer individuals a variety of potential areas to explore to find the best solution within the search space.

- Hunger role: Mathematical modeling is employed in this section to represent hunger-driven characteristics. Specifically, it quantifies the impact of hunger on each search step within the game environment. The calculation of the "weight of hunger," denoted as $\overrightarrow{W_1}$ and $\overrightarrow{W_2}$, is determined using the following Equations (Adel et al., 2022):

$$\overrightarrow{W_1} = \begin{cases} \text{hungry(i)} * \dfrac{N}{\text{SHungry}} * r_4, r_3 < 1 \\ 1, r_3 > 1 \end{cases} \tag{16}$$

$$\overrightarrow{W_2} = \left(1 - e^{-|\text{hungry(i)} - \text{hungry(i)}|}\right) * r_5 * 2 \tag{17}$$

In the given context, the hunger level of each agent is denoted by $h(i)$. *SHungry* represents the total hungry amount of all agents. The variable N indicates the total number of agents. Additionally, r_3, r_4, and r_5 are random numbers that fall within the range of [0,1].

- After evaluating the stop conditions, the optimal solution is returned if they are met. If the stop conditions are not met, the process of upgrading is repeated

3.8. Validation metrics

In this research, the validation is done in two steps. In step 1, various performance metrics were utilized to quantify the accuracy and predictive power of the optimized TabNet model. Commonly used metrics include RMSE (Equation (9)), MAE (Equation (18)), and R^2 coefficient (Equation (19)) (Farhangi et al., 2022; Razavi-Termeh et al., 2023).

$$\text{MAE} = \frac{\sum_{i=1}^{N} \left| y_i' - y_i \right|}{N} \tag{18}$$

$$R^2 = 1 - \frac{\text{SSR}}{\text{SST}} \tag{19}$$

In summary, in the context of these equations, n represents the total number of data points. The variable y_i represents the actual values, while y_i' represents the predicted values. The SSR is calculated by adding up all of the squared discrepancies between observed and forecasted data. Also, SST equals the total of the squared deviations from the actual values' mean. Step 2 involves assessing the quality of the susceptibility maps using the area under the ROC curve (AUC). To ensure reliable predictions, verifying any predictive model before its practical application is essential (Farahani et al., 2023). The ROC is a valuable

technique for evaluating the performance of detection systems. The AUC serves as a measure to assess the quality of the forecasting system. It characterizes the system's capability to accurately predict events, regardless of their occurrence or pre-determined nature (Masroor et al., 2023). The ROC curve depicts the relationship between the true positive rate (TPR) or sensitivity and the false positive rate (FPR) or 1-specificity along the X-axis. In terms of structure, the ROC curve follows a trajectory from the lower left corner to the upper right corner, forming a diagonal line. This curve is divided into two segments: the left portion represents thresholds associated with excellent performance (conservative), and the right segment corresponds to thresholds indicating poor decision-making (Uddin et al., 2023c). According to Yesilnacar and Topal (2005), the accuracy of spatial model prediction can be evaluated based on the relationship between the AUC and its corresponding classification. The model's accuracy is poor for AUC values ranging from 0.5 to 0.6. Moving to AUC values between 0.6 and 0.7, the accuracy is classified as medium. The model's accuracy is good because the AUC values fall between 0.7 and 0.8. Advancing further to AUC values ranging from 0.8 to 0.9, the accuracy is considered very good. Finally, the accuracy is excellent for AUC values between 0.9 and 1 (Shabanpour et al., 2022).

4. Results

4.1. Result of multicollinearity test

A multicollinearity analysis was conducted to assess the presence of multicollinearity among the predictor variables. The results of this analysis are summarized in Table 2. Among the evaluated criteria, the criterion of distance from the river exhibited the lowest VIF value of 1.01, indicating a negligible presence of multicollinearity. On the other hand, the bulk density criterion showed the highest VIF value of 5.56, suggesting a moderate level of multicollinearity. Despite this intermediate level, it does not exceed the threshold of 10, indicating that the bulk density criterion can still be included in the modeling process. Based on these results, all the parameters examined in this study demonstrated VIF values below 10, indicating that multicollinearity is not a significant concern. Consequently, all the parameters can be effectively incorporated into the modeling process.

4.2. Weight determination of effective criteria

The WOE method was employed to assess the relative importance of different criteria in influencing the occurrence of dust. Fig. 8 illustrates the weights assigned to each factor. Among the wind speed criteria, the 13–15 m/s class exhibited the highest impact on dust occurrence, with a WOE value 10.74. In the rainfall criterion, the 195–230 mm class demonstrated the most significant effect (WOE = 9.56). Regarding the Clay criterion, the 0–11 class was more influential, with a WOE value 12.04. Similarly, the soil water content criterion highlighted the significance of the 0–5 class, with a weight of 12.23. In the Sand criterion, the 64–95 class obtained the highest weight (WOE = 16.44). The 140–147 class emerged as the most important for the bulk density criterion, weighing 9.39. The altitude criterion indicated that the -23-160 m class had the most significant impact (WOE = 12.37). The NDVI criterion results identified the −0.08 to −0.06 class as having the highest weight, with a value of 16.63. Regarding the distance from the river criterion, the 300–400 m class was deemed the most critical (WOE = 0.98). Regarding the slope criterion, the 0–3° class exhibited the highest weight of 9.13. Entisols (WOE = 13.85) and Sandy loam (WOE = 7.68) were the most significant soil order and texture criteria, respectively. The slope aspect criterion highlighted the importance of the South East class, with a weight of 3.3. Lastly, the land cover and lithology criteria revealed the Clay (WOE = 12.77) and Qft2 (WOE = 14.4) classes to be the most influential, respectively.

Table 2
Multicollinearity analysis results.

Factors	Tolerance	VIF
Lithology	0.26	3.8
Land cover	0.56	1.77
Aspect	0.94	1.05
Soil texture	0.55	1.81
Slope	0.34	2.9
Distance to river	0.98	1.01
Altitude	0.56	1.76
Bulk density	0.18	5.56
Sand	0.87	1.13
Soil water content	0.45	2.18
Clay	0.45	2.19
Rainfall	0.47	2.09
Wind speed	0.52	1.9
Soil order	0.45	2.2
NDVI	0.24	4.11

4.3. Optimization and development of hybrid models

Next we showcase the outcomes of the modeling process by employing the TabNet model in conjunction with three metaheuristic algorithms: PSO, GWO, and HGS. The WOE method's output weights were used as inputs, with values for each criterion normalized to lie between 0 and 1. To facilitate the modeling process, the control parameters of the three metaheuristic algorithms were defined, as shown in Table 3.

The modeling and optimization procedures were implemented using Python programming in the Google Colab platform. The experiments were conducted on a computer system running on Windows 10 64-bit, equipped with an Intel(R) Core(TM) i7 CPU and 16 GB of RAM. The three metaheuristic algorithms were employed to optimize the hyperparameters of the TabNet algorithm. Each algorithm utilized a population of 50 and underwent 100 optimization process cycles. The objective of the optimization process was to minimize the RMSE index, which serves as the performance evaluation metric. Fig. 9 illustrates the convergence functions of the three metaheuristic algorithms. HGS, PSO, and GWO achieved objective function values of 0.105, 0.113, and 0.176, respectively, indicating superior performance in optimizing the TabNet algorithm. The optimized values of the TabNet hyperparameters resulting from the metaheuristic algorithm optimizations are presented in Table 4.

Fig. 10 displays the outcomes of assessing the significance of critical criteria utilizing the TabNet model. Results showed that the most important criteria were wind speed, soil texture, and altitude. In contrast, the parameters of distance from the river, slope aspect, and soil order had relatively lower importance in determining dust occurrence.

The performance of the four TabNet models (TabNet, TabNet-GWO, TabNet-PSO, and TabNet-HGS) was evaluated using training and testing data. Fig. 11 illustrates the modeling results based on statistical indicators. Regarding statistical indicators in the training data, the TabNet-HGS model demonstrated the highest accuracy, with RMSE = 0.1, MAE = 0.055, and R^2 = 0.959. It was followed by the TabNet-PSO models, with RMSE = 0.138, MAE = 0.073, and R^2 = 0.923. The TabNet-GWO model achieved RMSE = 0.167, MAE = 0.08, and R^2 = 0.888, while the TabNet model obtained RMSE = 0.197, MAE = 0.109, and R^2 = 0.844. The performance rankings in the testing data were similar to the training data. The TabNet-HGS model exhibited the highest accuracy, with RMSE = 0.114, MAE = 0.063, and R^2 = 0.947. The TabNet-PSO models achieved RMSE = 0.145, MAE = 0.081, and R^2 = 0.907. The TabNet-GWO model obtained RMSE = 0.176, MAE = 0.096, and R^2 = 0.875, while the TabNet model yielded RMSE = 0.187, MAE = 0.121, and R^2 = 0.858. These results indicate that integrating metaheuristic algorithms with the TabNet model improves accuracy compared to the standalone TabNet model. The HGS algorithm demonstrated the highest accuracy in training and testing data among the metaheuristic

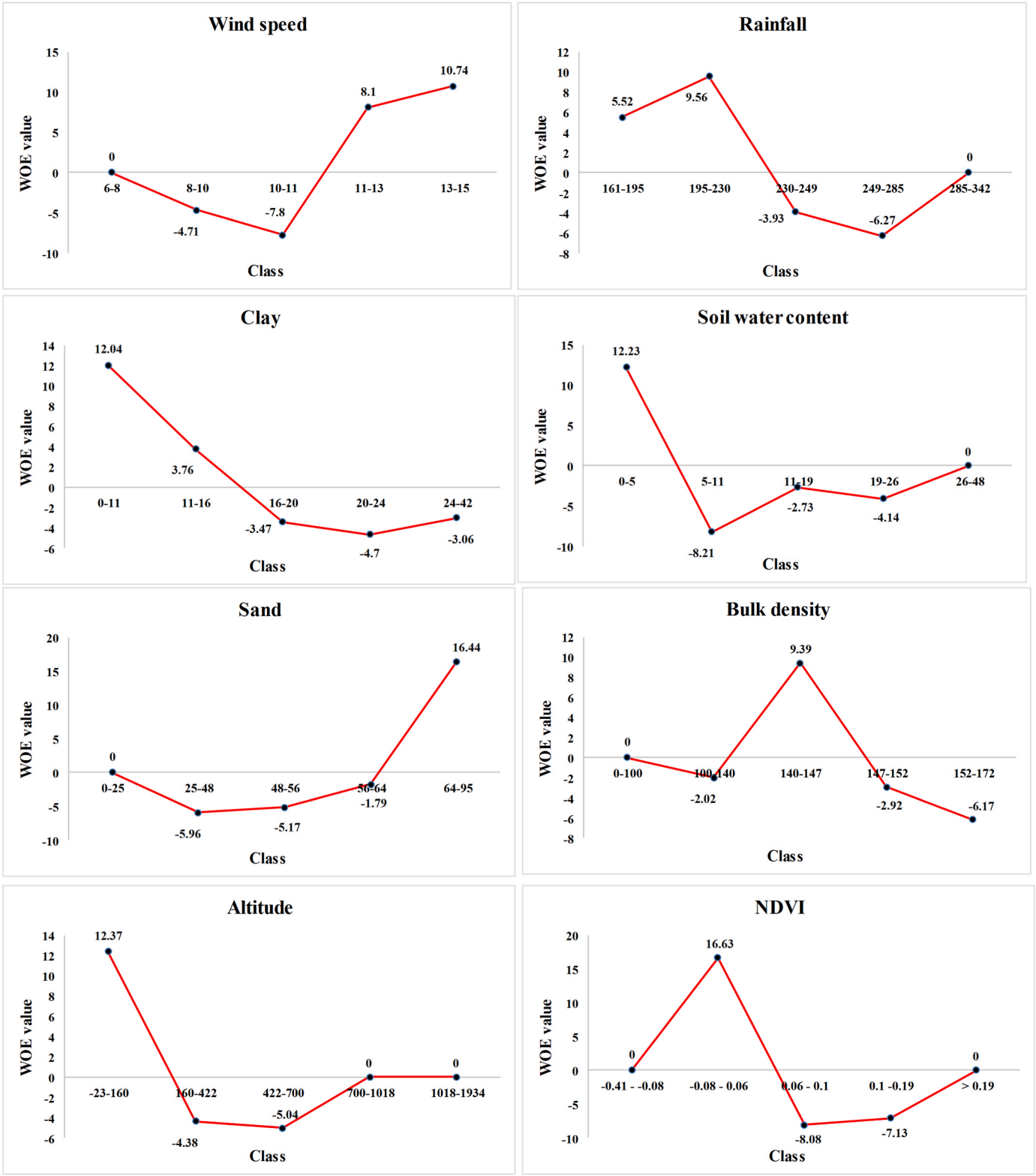

Fig. 8. Assessment of weight factors for effective dust criteria.

algorithms.

Fig. 12 and Table 5 present the results related to the prediction error of the four models: TabNet, TabNet-GWO, TabNet-PSO, and TabNet-HGS. The prediction error was assessed based on the training and test data's mean values and standard deviation (STD). For the TabNet model, the mean prediction error was −0.00028 in the training data. The TabNet-GWO model exhibited a mean error of −0.02, while the TabNet-PSO and TabNet-HGS models showed mean errors of −0.013 and 0.0032, respectively. In the test data, the mean prediction errors were as follows: TabNet (−0.059), TabNet-GWO (0.0093), TabNet-PSO

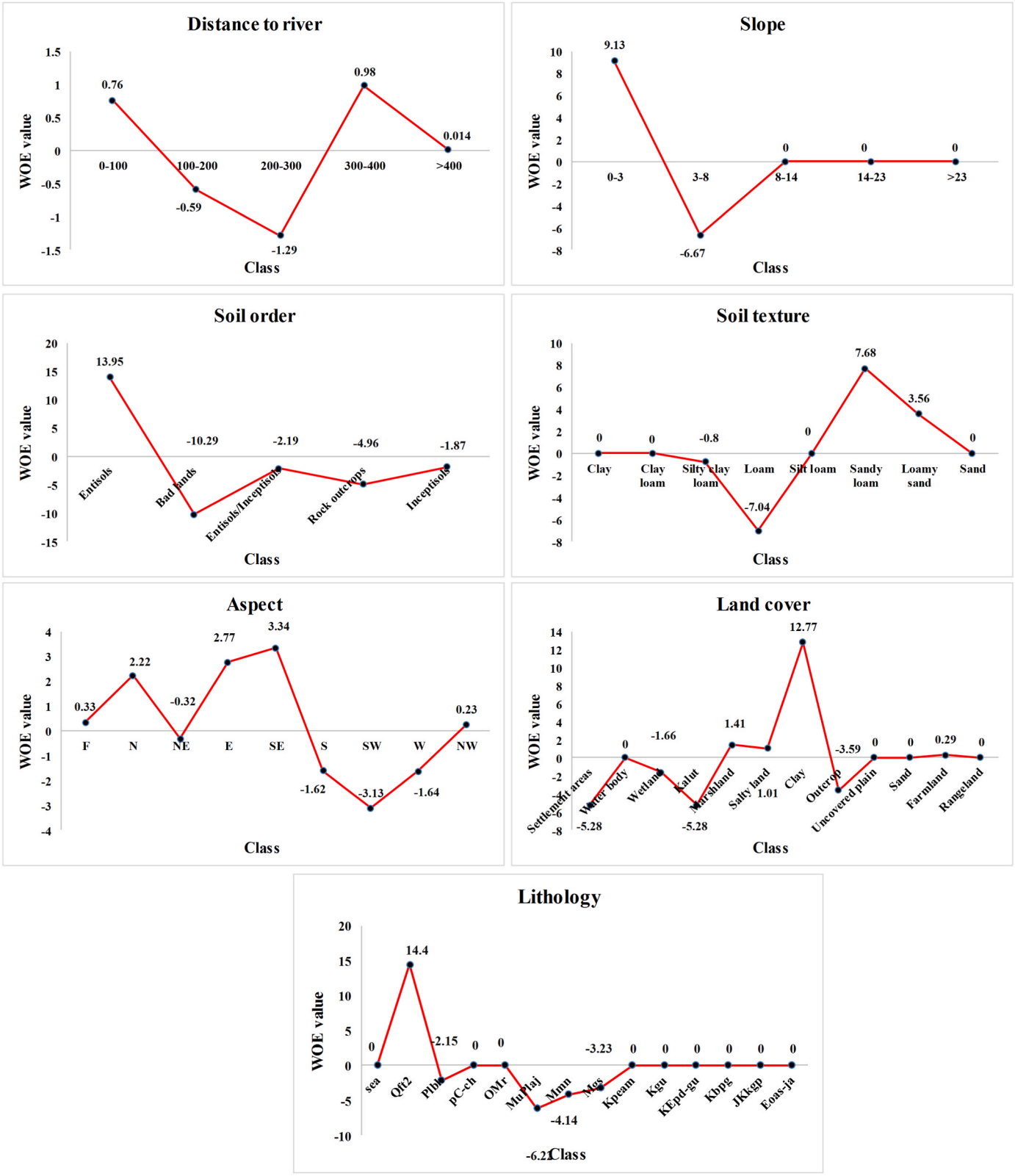

Fig. 8. (*continued*).

(−0.012), and TabNet-HGS (0.0057). In the training data, the lowest STD was observed in the TabNet-HGS model (0.1), followed by TabNet-PSO (0.137), TabNet-GWO (0.165), and TabNet (0.197). In the test data, the STD values were TabNet-HGS (0.105), TabNet-PSO (0.114), TabNet-GWO (0.175), and TabNet (0.177). The TabNet-HGS model exhibited the lowest mean error and STD, indicating its superior performance in predicting dust occurrences.

Table 3
Parameter control of swarm-based algorithms.

Algorithms	Parameters
PSO	Population = 50 Iteration = 100 Local coefficient = 2.05 Global coefficient = 2.05 Weight min of particle = 0.4 Weight max of particle = 0.9
HGS	Population = 50 Iteration = 100 The probability of updating position = 0.08 Largest hunger = 10000
GWO	Population = 50 Iteration = 100

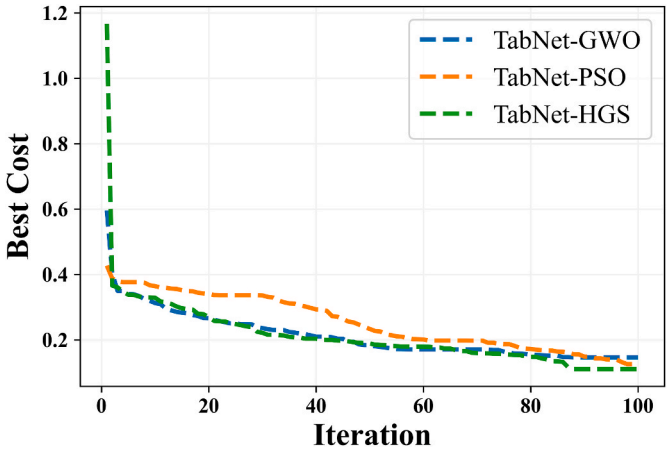

Fig. 9. Convergence diagram of TabNet optimization.

4.4. Develop a dust susceptibility map (DSM)

To generate the DSM, the four models developed were applied to the entire Bushehr province. The resulting susceptibility maps, shown in Fig. 13, were scaled between 0 and 1, with values close to 1 indicating higher susceptibility to dust. The Natural breaks classification method was employed to categorize the risk levels, resulting in the qualitative division of the susceptibility maps into five classes: very low risk, low risk, medium risk, high risk, and very high risk. According to the susceptibility maps, the western and southern regions of the province exhibited greater susceptibility to dust. Although the susceptibility classes assigned by the four models were similar, it is worth noting that the TabNet model differed in structure from the hybrid models.

The distribution of susceptibility classes for all four models is presented in Fig. 14. Among the four models, the highest percentages of very low, low, moderate, high, and very high-risk classes were observed in the following order: TabNet-HGS (48.36%), TabNet-GWO (45.12%), TabNet-PSO (30.82%), TabNet (28.69%), and TabNet-GWO (29.45%). Furthermore, when considering the combined "High + Very High" risk classes, the TabNet-GWO model had the highest percentage (48.36%), followed by TabNet-HGS (45.12%), TabNet-PSO (30.82%), and TabNet (28.69%). These findings demonstrate the efficacy of the models in assessing the susceptibility of different areas within Bushehr province to dust, with the hybrid algorithms (TabNet-HGS and TabNet-GWO) consistently outperforming the standalone TabNet model in predicting higher risk levels.

4.5. Comparison and validation of susceptibility maps

To assess the accuracy of the susceptibility maps about real-world data, 30% of the dust occurrence data, which was not used in the modeling process, was employed. Fig. 15 and Table 6 show the ROC curve and AUC results, respectively, for the evaluation. The AUC values demonstrated the modeling accuracy of each approach. The TabNet-HGS model exhibited the highest accuracy with an AUC of 0.994, followed by TabNet-PSO with an AUC of 0.986, TabNet-GWO with an AUC of 0.980, and the standalone TabNet model with an AUC of 0.832. These results indicate that incorporating metaheuristic algorithms based on Swarm optimization enhanced the accuracy of the TabNet model. Specifically, the HGS algorithm improved the accuracy of the TabNet model by 16.2%, the PSO algorithm by 15.4%, and the GWO algorithm by 14.8%. Among the metaheuristic algorithms, the HGS algorithm demonstrated higher accuracy in optimizing the TabNet model than

Table 4
Optimized TabNet hyperparameters.

Algorithms	n_d	n_a	n_steps	gamma	n_independent	n_shared	momentum
HGS	26	24	4	1.14	4	1	0.058
PSO	20	8	3	1	1	1	0.102
GWO	8	8	4	1	5	3	0.4

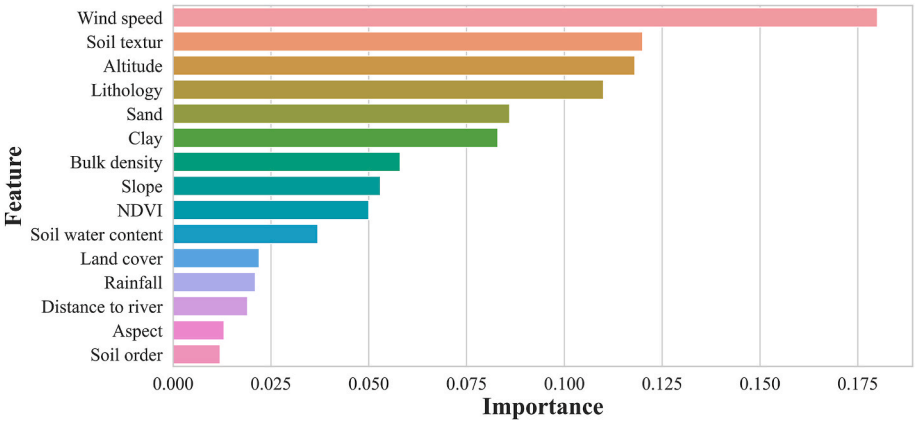

Fig. 10. Features importance using TabNet model.

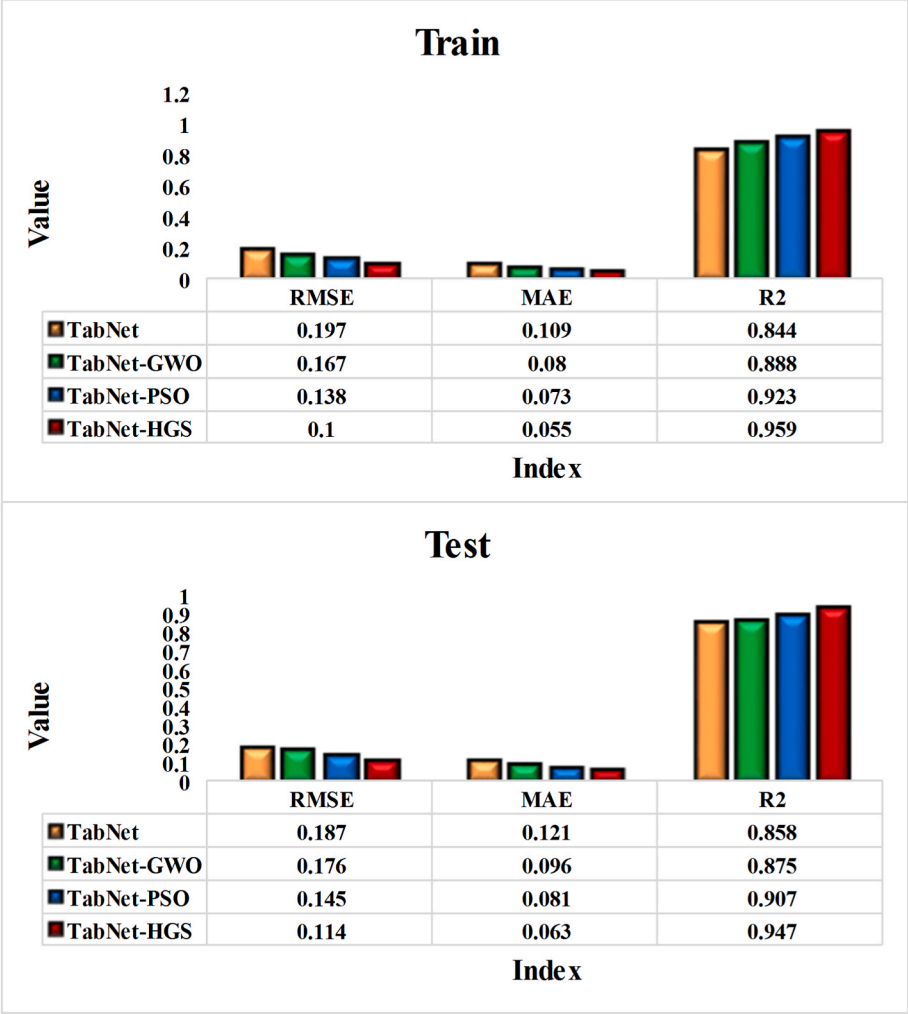

Fig. 11. Performance comparison of four TabNet-based models.

GWO and PSO. These findings validate the effectiveness of incorporating Swarm-based metaheuristic algorithms in improving the modeling accuracy of the TabNet approach for DSM. The HGS algorithm outperformed GWO and PSO, highlighting its suitability for optimizing the TabNet model in this context.

5. Discussion

5.1. Key findings regarding effective dust factors

In our study, we employed the WOE method to assess the probability of dust occurrence in each class of the practical criteria. The WOE method allowed us to quantify the relationship between the criteria and the likelihood of dust events while unifying our modeling approach's input criteria. The results of our analysis indicated that areas characterized by elevated wind speeds had a greater likelihood of experiencing dust events, consistent with general expectations (Prospero et al., 2002). Stronger winds facilitate the movement and scattering of dust particles, resulting in heightened dust concentrations in the impacted regions (Mani and Pillai, 2010). Based on the findings of our study, there was a higher probability of dust occurrence in Bushehr province when lower amounts of rainfall were recorded, which translates to reduced soil moisture promoting more dust erosion (Gillette, 1999; Kavouras et al., 2007), leading to increased dust generation and transport in the area (Achakulwisut et al., 2017). Consistent with the previous result, the WOE analysis demonstrated that areas with lower soil water content had a greater likelihood of experiencing dust events. Considering these factors, the influence of lower soil water content criterion on dust occurrence is amplified due to its contribution to soil instability, heightened generation of dust particles, sparse vegetation cover, and insufficient water availability for dust suppression. These combined effects make areas with lower soil water content more susceptible to dust events (Leung et al., 2022).

Our analysis revealed that areas with lower clay content had a greater probability of experiencing dust events. This suggests that a reduction in clay levels can contribute to soil erosion and the generation of dust particles (Zucca et al., 2021). Consequently, regions with lower amounts of clay are more susceptible to dust occurrences. Our results found that higher values of the Sand criterion had a high impact on dust occurrence. This implies that an increase in sand levels can contribute to soil erosion and the generation of dust particles, thus enhancing dust events (Cao et al., 2015a,b). Our findings showed that the intermediate values (140–147) of the Bulk density criterion promoted the occurrence of dust. This suggests an optimal Bulk density range where soil conditions are more conducive to dust generation and transport (Sahu and Mishra, 2023). The results of our study indicated that dust occurrences were more likely to happen at lower altitudes. This can be attributed to atmospheric stability, wind patterns, and dust sources. At lower altitudes, air masses tend to be more stable, facilitating the accumulation and transport of dust particles (Sun et al., 2018). Additionally, the proximity to potential dust sources, such as arid regions or human activities, may contribute to higher dust events at lower elevations

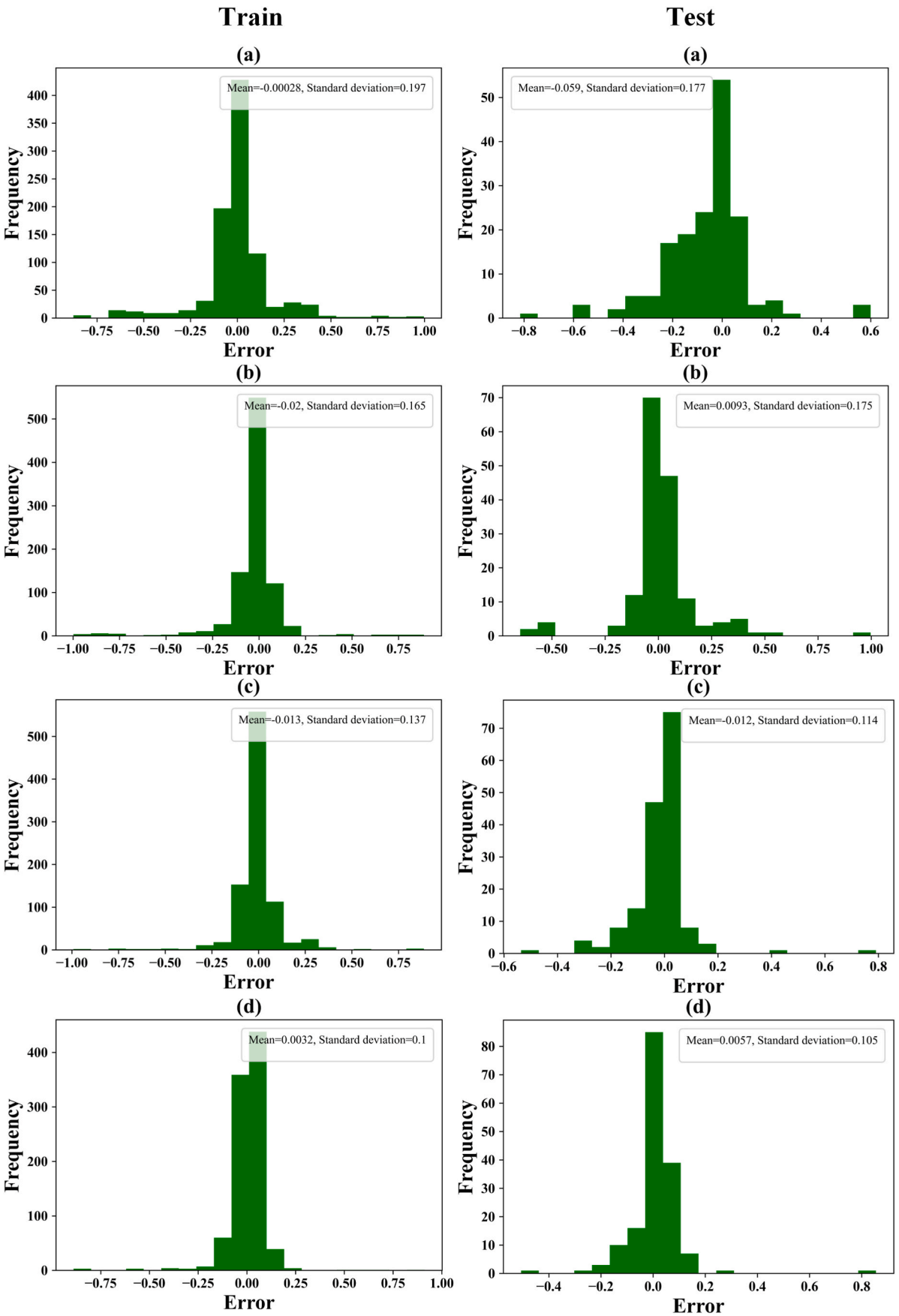

Fig. 12. Prediction error diagram of four TabNet-based models: a) TabNet, b) TabNet-GWO, c) TabNet-PSO, and d) TabNet-HGS.

Table 5
Prediction error analysis of four TabNet-based models.

Models	Train		Test	
	Mean	STD	Mean	STD
TabNet	−0.00028	0.197	−0.059	0.177
TabNet-GWO	−0.02	0.165	0.0093	0.175
TabNet-PSO	−0.013	0.137	−0.012	0.114
TabNet-HGS	0.0032	0.1	0.0057	0.105

(Reynolds et al., 2001).

According to our study's methodology, we discovered that lower values of the NDVI criterion had a more pronounced effect on dust occurrence, consistent with past work showing a similar relationship over the Middle East (Namdari et al., 2022). In regions with lower NDVI values, the vegetation cover tended to be sparse or less robust, exposing the soil and making it more susceptible to erosion (Mallick et al., 2014). Low vegetation exacerbates the generation of dust particles and hampers dust suppression efforts by reducing the protective barrier against wind erosion (Brantley et al., 2014). According to the results of our study, dust occurrences were found to be more likely at a distance of 300–400 m from the river. Rivers often significantly impact the local environment, influencing soil moisture levels, sediment deposition, and vegetation patterns (Wang et al., 2021). Areas closer to the river may exhibit specific characteristics that make them more prone to dust generation and transport. Additionally, sediment deposition from the river can alter soil properties, potentially affecting dust dynamics in nearby areas (Von Holdt et al., 2017). Our findings determined that lower values of the slope criterion had a more significant effect on the occurrence of dust. There are several reasons why lower slope values can contribute to increased dust occurrence. Firstly, flatter terrain tends to have reduced surface roughness, allowing for more accessible dust particle transport by wind (Boroughani et al., 2021). Additionally, lower-slope areas may experience reduced water runoff, leading to drier soil conditions and increased dust generation (Cheng et al., 2008). According to our results, the analysis of soil orders revealed that the Entisols class had a more significant impact on the occurrence of dust. Entisols often have limited soil structure and poor aggregation, making them more prone to erosion (Ogunwole et al., 2008). The lack of well-developed horizons and inadequate soil stabilization mechanisms can lead to easier detachment and transport of soil particles by wind, resulting in increased dust generation (Bhat et al., 2019). The results of the soil texture revealed that the sandy loam class had the most significant impact on the occurrence of dust, according to our findings. Sandy soils have a relatively loose structure, which makes them more susceptible to erosion and wind transport of soil particles (Duniway et al., 2019). A higher proportion of sand particles in sandy loam soils enhances their vulnerability to wind erosion and increases the likelihood of dust generation (Ding et al., 2018). Based on our findings, we observed a higher probability of dust in areas with a southeast slope aspect.

The influence of wind patterns and prevailing winds on the transport and dispersion of dust particles cannot be underestimated. In certain regions, the prevalence of southeast winds can result in the transportation of dust particles from specific source areas or parts conducive

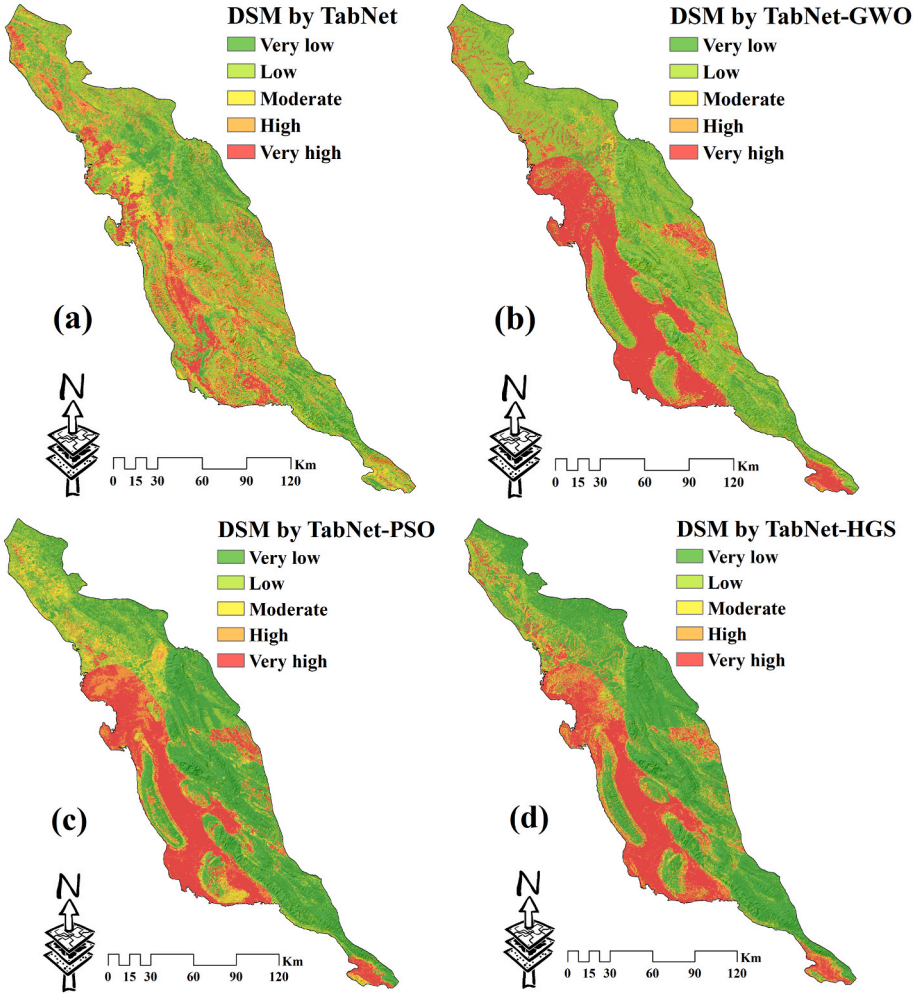

Fig. 13. Dust susceptibility mapping (DSM) by four TabNet-based models: a) TabNet, b) TabNet-GWO, c) TabNet-PSO, and d) TabNet-HGS.

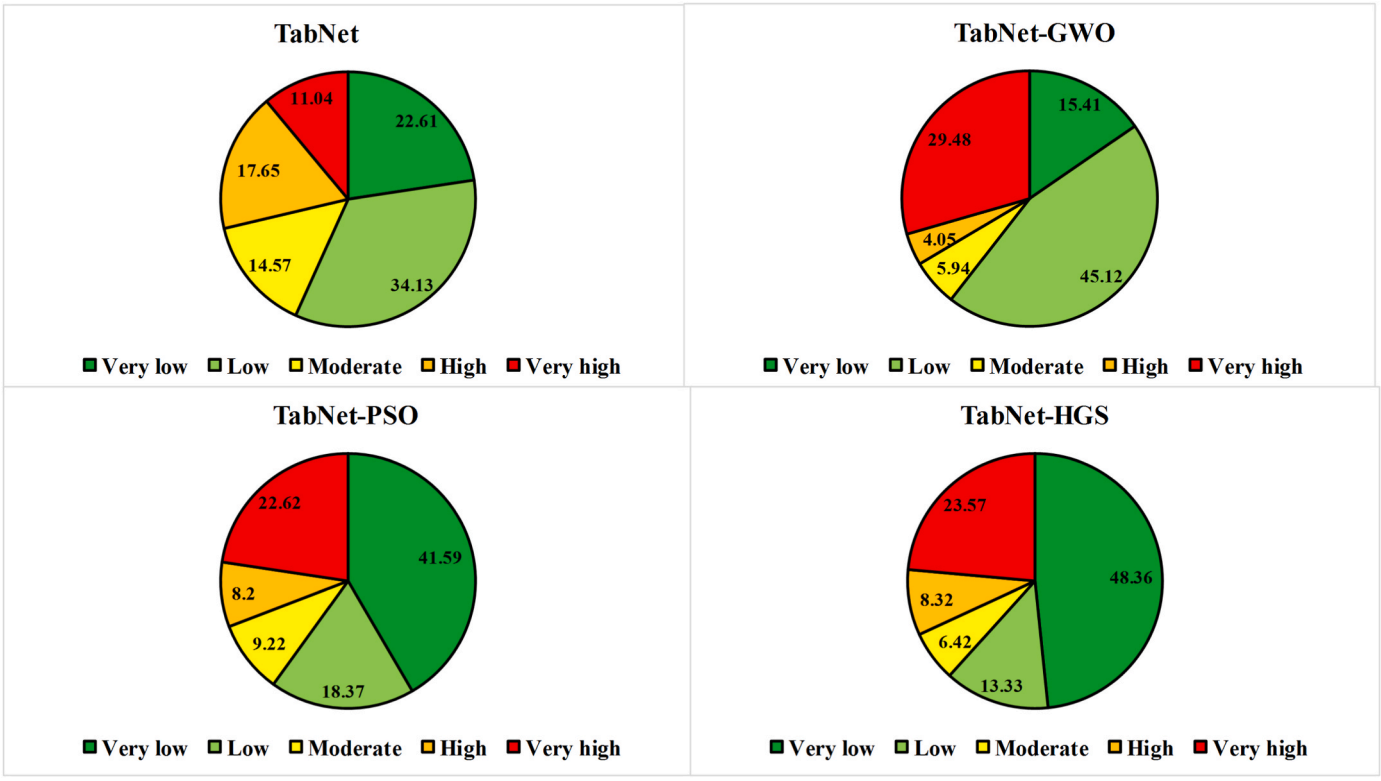

Fig. 14. Distribution of susceptibility classes of four TabNet-based models.

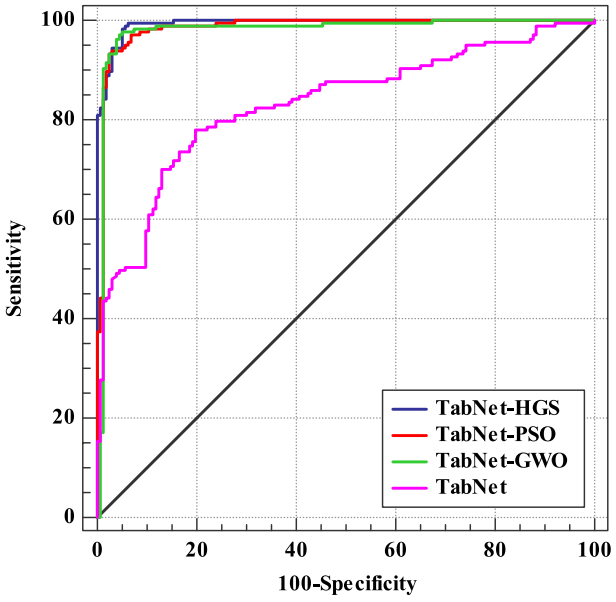

Fig. 15. Comparison of four dust susceptibility maps by ROC.

Table 6
Comparison of susceptibility maps of four TabNet-based models.

Models	AUC	Standard Error (SE)	95% CI
TabNet-HGS	0.994	0.00253	0.978 to 0.999
TabNet-PSO	0.986	0.00584	0.966 to 0.996
TabNet-GWO	0.980	0.00934	0.958 to 0.992
TabNet	0.832	0.0230	0.787 to 0.871

to dust generation (Bullard et al., 2016). Our study revealed that areas with clay land cover exhibited a higher likelihood of dust occurrences. Clay soils possess distinctive characteristics that significantly impact dust dynamics (Liu et al., 2020). With their fine-grained and cohesive nature, clay particles are susceptible to erosion and easily suspended by wind, ultimately generating and transporting dust particles across greater distances (Prokof'eva et al., 2017). Our findings indicate that the Qft2 lithology class had the most pronounced effect on dust occurrence. This particular lithological class exhibits distinct characteristics or compositions that render it more vulnerable to erosion and the production of dust particles. The specific features or composition of rocks or soil associated with the Qft2 class are likely responsible for its heightened influence on dust events (Gholami et al., 2020a,b,c).

The findings from the TabNet model emphasized the significance of wind speed, soil texture, and altitude as the primary factors in predicting dust occurrences within the study area. Higher wind speeds were identified as a significant parameter, indicating their role in facilitating the transport and dispersion of dust particles, resulting in elevated dust concentrations in the affected regions (Kedia et al., 2018). Furthermore, soil texture emerged as a crucial parameter, particularly emphasizing the impact of certain surfaces, such as sandy or loamy soils, on dust occurrence (Gherboudj et al., 2015). These soil types possess characteristics that make them more susceptible to erosion and the generation of dust particles, which the wind can easily carry (Rezaei et al., 2019).

Moreover, altitude was found to be an essential factor in predicting the occurrence of dust. Lower altitudes exhibited a higher probability of dust events, potentially due to variations in topography, air circulation patterns, and proximity to dust sources. These factors can fluctuate with altitude and influence the concentration and distribution of dust particles (Rashki et al., 2021).

5.2. Comparison of optimized models

In this study, three swarm-based metaheuristic algorithms were employed to enhance the performance of the TabNet model in predicting

dust occurrences and generating dust susceptibility maps. The algorithms used were the HGS, PSO, and GWO. The results from various statistical indicators demonstrated that the HGS algorithm outperformed the other two, namely PSO and GWO, in optimizing the TabNet model and generating more accurate dust susceptibility maps. Utilizing the HGS algorithm improved accuracy and precision in predicting areas prone to dust events. The HGS algorithm provides several advantages over the PSO and GWO algorithms. One key advantage is its ability to achieve a balanced exploration-exploitation tradeoff (Yang et al., 2021). By incorporating a pleasant memory, HGS maintains diverse solutions while exploring new regions of the search space. This dynamic balance helps prevent premature convergence and enables the algorithm to discover better solutions than PSO and GWO (Houssein et al., 2023). Another advantage of HGS is its robustness to parameter settings. Unlike PSO and GWO, which often require extensive parameter tuning, HGS demonstrates excellent stability and is less sensitive to parameter adjustments. This reduces the effort and time needed for parameter fine-tuning, making HGS easier to implement and use in practice (Mahajan et al., 2022). Following the HGS algorithm, the PSO algorithm exhibited higher accuracy than the GWO algorithm. Although the PSO algorithm did not perform as well as the HGS algorithm, it still demonstrated the capability to enhance the TabNet model's accuracy and contribute to developing reliable dust susceptibility maps. One significant advantage is the simplicity and ease of implementation of PSO (Juneja and Nagar, 2016). Its straightforward concept, involving the movement of particles in a search space, makes it easier to understand and apply than the GWO algorithm (Chen et al., 2009). Compared to GWO, PSO typically has fewer control parameters, simplifying the optimization process and reducing the need for extensive parameter tuning. It mainly involves setting the number of particles, inertia weight, and acceleration coefficients. This simplicity in parameter configuration adds to the ease of implementing and applying PSO (Juneja and Nagar, 2016).

5.3. Limitations and recommendations

While our study successfully employed satellite-based dust monitoring and the optimization of the TabNet model using swarm-based metaheuristic algorithms, several limitations must be acknowledged. These limitations present opportunities for further research and improvements in future studies. One of the primary limitations encountered in this research was the low spatial resolution of the MODIS images. In the case of MODIS images, more than the spatial resolution might be required to capture fine-scale variations in dust concentrations or accurately assess the spatial distribution of dust events. The satellite imagery's low spatial resolution can aggregate dust data over larger areas, potentially masking localized variations or small-scale dust events. This limitation can affect dust monitoring and susceptibility mapping accuracy and precision, particularly in regions with heterogeneous landscapes or where dust events exhibit localized patterns. To overcome this limitation, future research could explore using satellite sensors with higher spatial resolution, such as commercial high-resolution optical or radar satellites and downscaling methods. Another significant limitation of our study was the need for more access to dust field validation and ground truthing data. While satellite-based monitoring and modeling techniques provide valuable insights, it is essential to validate the accuracy and reliability of the results through field surveys and ground-level data collection. Unfortunately, we could not conduct extensive field validation and ground truthing during this research due to various logistical and resource constraints. The lack of access to such data limits the ability to thoroughly verify and validate the satellite observations and model outputs, introducing uncertainties in the accuracy of the findings. Future research should prioritize collecting field validation and ground-truthing data to address this limitation. Field surveys can be conducted to measure dust concentrations at specific locations, collect soil samples for laboratory analysis, and gather meteorological data to complement satellite-based observations. This will provide a robust foundation for verifying the accuracy of the satellite data and improving the reliability of the dust monitoring and susceptibility mapping results. Also, future research can address the spatio-temporal modeling of dust and pay attention to its temporal patterns.

6. Conclusion and remarks

This study employed satellite-based dust monitoring and optimized the TabNet model using swarm-based metaheuristic algorithms to investigate the factors influencing dust occurrence and create a dust susceptibility map. The findings provide valuable insights into influential dust factors and contribute to understanding and mitigating dust events in the study area. Using the WOE method, several significant factors influencing dust occurrence were identified, which are consistent with general expectations from literature providing high confidence in the methods employed in this work. High wind speeds enhanced dust transport and dispersion, resulting in an increased probability of dust occurrence. Additionally, lower levels of rainfall, clay content, soil water content, altitude, slope, distance to the river, and NDVI values were associated with a higher likelihood of dust events, indicating their contribution to soil erosion, dust particle generation, and reduced vegetation cover. Clay land cover, Qft2 lithology, Entisols soil texture, and SouthEast aspect influenced dust occurrence. Optimizing the TabNet model using swarm-based metaheuristic algorithms, including the HGS, PSO, and GWO, demonstrated their effectiveness in improving model accuracy and developing a robust DSM. Among these algorithms, the HGS algorithm outperformed the PSO and GWO algorithms in optimizing the TabNet model and producing accurate susceptibility maps. The findings of this research have practical implications for policymakers, land managers, and stakeholders involved in dust control and prevention efforts in the study area and similar regions. The identified factors can inform the development of targeted measures to mitigate dust events and protect the environment.

CRediT authorship contribution statement

Seyed Vahid Razavi-Termeh: Writing – original draft, Visualization, Software, Methodology, Investigation, Formal analysis, Data curation, Conceptualization. **Abolghasem Sadeghi-Niaraki:** Writing – review & editing, Supervision, Resources, Project administration, Methodology, Investigation. **Armin Sorooshian:** Writing – review & editing, Validation, Methodology, Resources. **Tamer Abuhmed:** Writing – review & editing, Validation, Resources, Visualization. **Soo-Mi Choi:** Writing – review & editing, Validation, Supervision, Project administration, Funding acquisition, Methodology.

Declaration of competing interest

The authors declare that they have no known competing financial interests or personal relationships that could have appeared to influence the work reported in this paper.

Data availability

Data will be made available on request.

Acknowledgements

This work was supported in part by the ITRC Support Program under Grant IITP-2024-RS-2022-00156354 and in part by the Metaverse Support Program to Nurture the Best Talents under Grant IITP-2024-RS-2023-00254529 funded by the Ministry of Science and ICT of Korea and the Institute of Information and Communications Technology Planning and Evaluation (IITP) and in part by the Ministry of Trade, Industry and

Energy and Korea Institute for Advancement of Technology under Grant P0016038.

Appendix A. Supplementary data

Supplementary data to this article can be found online at https://doi.org/10.1016/j.jenvman.2024.120682.

References

Abdalla, T.E., Peng, C., 2021. Evaluation of housing stock indoor air quality models: a review of data requirements and model performance. J. Build. Eng. 43, 102846.

Achakulwisut, P., Shen, L., Mickley, L.J., 2017. What controls springtime fine dust variability in the western United States? Investigating the 2002–2015 increase in fine dust in the US Southwest. J. Geophys. Res. Atmos. 122 (22), 12–449.

Adel, H., Dahou, A., Mabrouk, A., Abd Elaziz, M., Kayed, M., El-Henawy, I.M., et al., 2022. Improving crisis events detection using distilbert with hunger games search algorithm. Mathematics 10 (3), 447.

Allen, C.J., Washington, R., Saci, A., 2015. Dust detection from ground-based observations in the summer global dust maximum: results from Fennec 2011 and 2012 and implications for modeling and field observations. J. Geophys. Res. Atmos. 120 (3), 897–916.

An, L., Che, H., Xue, M., Zhang, T., Wang, H., Wang, Y., et al., 2018. Temporal and spatial variations in sand and dust storm events in East Asia from 2007 to 2016: relationships with surface conditions and climate change. Sci. Total Environ. 633, 452–462.

Arik, S.Ö., Pfister, T., 2021. Tabnet: attentive interpretable tabular learning. May. In: Proceedings of the AAAI Conference on Artificial Intelligence, vol. 35, pp. 6679–6687, 8.

Asencios, R., Asencios, C., Ramos, E., 2023. Profit scoring for credit unions using the multilayer perceptron, XGBoost and TabNet algorithms: evidence from Peru. Expert Syst. Appl. 213, 119201.

Ayanu, Y.Z., Conrad, C., Nauss, T., Wegmann, M., Koellner, T., 2012. Quantifying and mapping ecosystem services supplies and demands: a review of remote sensing applications. Environ. Sci. Technol. 46 (16), 8529–8541.

Baddock, M.C., Bryant, R.G., Acosta, M.D., Gill, T.E., 2021. Understanding dust sources through remote sensing: making a case for CubeSats. J. Arid Environ. 184, 104335.

Balogun, A.L., Tella, A., Baloo, L., Adebisi, N., 2021. A review of the inter-correlation of climate change, air pollution and urban sustainability using novel machine learning algorithms and spatial information science. Urban Clim. 40, 100989.

Batar, A.K., Watanabe, T., 2021. Landslide susceptibility mapping and assessment using geospatial platforms and weights of evidence (WoE) method in the Indian Himalayan Region: recent developments, gaps, and future directions. ISPRS Int. J. Geo-Inf. 10 (3), 114.

Bernardo, L.S., Damaševičius, R., De Albuquerque, V.H.C., Maskeliūnas, R., 2021. A hybrid two-stage SqueezeNet and support vector machine system for Parkinson's disease detection based on handwritten spiral patterns. Int. J. Appl. Math. Comput. Sci. 31 (4), 549–561.

Bhat, S.A., Dar, M.U.D., Meena, R.S., 2019. Soil erosion and management strategies. Sustainable Management of Soil and Environment 73–122.

Binitha, S., Sathya, S.S., 2012. A survey of bio inspired optimization algorithms. Int. J. Soft Comput. Eng. 2 (2), 137–151.

Boloorani, A.D., Shorabeh, S.N., Samany, N.N., Mousivand, A., Kazemi, Y., Jaafarzadeh, N., et al., 2021. Vulnerability mapping and risk analysis of sand and dust storms in Ahvaz, Iran. Environ. Pollut. 279, 116859.

Boroughani, M., Pourhashemi, S., Gholami, H., Kaskaoutis, D.G., 2021. Predicting of dust storm source by combining remote sensing, statistic-based predictive models and game theory in the Sistan watershed, southwestern Asia. Journal of Arid Land 13 (11), 1103–1121.

Boroughani, M., Pourhashemi, S., Hashemi, H., Salehi, M., Amirahmadi, A., Asadi, M.A. Z., Berndtsson, R., 2020. Application of remote sensing techniques and machine learning algorithms in dust source detection and dust source susceptibility mapping. Ecol. Inf. 56, 101059.

Brantley, H.L., Hagler, G.S., Deshmukh, P.J., Baldauf, R.W., 2014. Field assessment of the effects of roadside vegetation on near-road black carbon and particulate matter. Sci. Total Environ. 468, 120–129.

Broomandi, P., Karaca, F., Guney, M., Fathian, A., Geng, X., Kim, J.R., 2021. Destinations frequently impacted by dust storms originating from southwest Iran. Atmos. Res. 248, 105264.

Bullard, J.E., Baddock, M., Bradwell, T., Crusius, J., Darlington, E., Gaiero, D., et al., 2016. High-latitude dust in the Earth system. Rev. Geophys. 54 (2), 447–485.

Cao, H., Amiraslani, F., Liu, J., Zhou, N., 2015a. Identification of dust storm source areas in West Asia using multiple environmental datasets. Sci. Total Environ. 502, 224–235.

Cao, H., Liu, J., Wang, G., Yang, G., Luo, L., 2015b. Identification of sand and dust storm source areas in Iran. Journal of Arid Land 7, 567–578.

Chen, Q., Guo, W., Li, C., 2009. An improved PSO algorithm to optimize BP neural network. In: 2009 Fifth International Conference on Natural Computation, vol. 2. IEEE, pp. 357–360. August.

Cheng, Q., Ma, W., Cai, Q., 2008. The relative importance of soil crust and slope angle in runoff and soil loss: a case study in the hilly areas of the Loess Plateau, North China. Geojournal 71, 117–125.

Choubin, B., Hosseini, F.S., Rahmati, O., Youshanloei, M.M., Jalali, M., 2023. Mapping of salty aeolian dust-source potential areas: ensemble model or benchmark models? Sci. Total Environ. 877, 163419.

Darvishi Boloorani, A., Soleimani, M., Neysani Samany, N., Bakhtiari, M., Qareqani, M., Papi, R., Mirzaei, S., 2023. Assessment of rural vulnerability to sand and dust storms in Iran. Atmosphere 14 (2), 281.

Ding, X., Xu, G., Kizil, M., Zhou, W., Guo, X., 2018. Lignosulfonate treating bauxite residue dust pollution: enhancement of mechanical properties and wind erosion behavior. Water, Air, Soil Pollut. 229, 1–13.

Duniway, M.C., Pfennigwerth, A.A., Fick, S.E., Nauman, T.W., Belnap, J., Barger, N.N., 2019. Wind erosion and dust from US drylands: a review of causes, consequences, and solutions in a changing world. Ecosphere 10 (3), e02650.

Fahim, S.R., Hasanien, H.M., Turky, R.A., Alkuhayli, A., Al-Shamma'a, A.A., Noman, A. M., et al., 2021. Parameter identification of proton exchange membrane fuel cell based on hunger games search algorithm. Energies 14 (16), 5022.

Farahani, M., Razavi-Termeh, S.V., Sadeghi-Niaraki, A., 2022. A spatially based machine learning algorithm for potential mapping of the hearing senses in an urban environment. Sustain. Cities Soc. 80, 103675.

Farahani, M., Razavi-Termeh, S.V., Sadeghi-Niaraki, A., Choi, S.M., 2023. People's olfactory perception potential mapping using a machine learning algorithm: a Spatio-temporal approach. Sustain. Cities Soc. 93, 104472.

Farhangi, F., Sadeghi-Niaraki, A., Nahvi, A., Razavi-Termeh, S.V., 2022. Spatial modelling of accidents risk caused by driver drowsiness with data mining algorithms. Geocarto Int. 37 (9), 2698–2716.

Franke, G.R., 2010. Multicollinearity. Wiley international encyclopedia of marketing.

Gadekallu, T.R., Alazab, M., Kaluri, R., Maddikunta, P.K.R., Bhattacharya, S., Lakshmanna, K., 2021. Hand gesture classification using a novel CNN-crow search algorithm. Complex & Intelligent Systems 7, 1855–1868.

Gherboudj, I., Beegum, S.N., Marticorena, B., Ghedira, H., 2015. Dust emission parameterization scheme over the MENA region: sensitivity analysis to soil moisture and soil texture. J. Geophys. Res. Atmos. 120 (20), 10–915.

Gholami, H., Mohamadifar, A., Sorooshian, A., Jansen, J.D., 2020a. Machine-learning algorithms for predicting land susceptibility to dust emissions: the case of the Jazmurian Basin, Iran. Atmos. Pollut. Res. 11 (8), 1303–1315.

Gholami, H., Mohamadifar, A., Collins, A.L., 2020b. Spatial mapping of the provenance of storm dust: application of data mining and ensemble modelling. Atmos. Res. 233, 104716.

Gholami, H., Mohammadifar, A., Pourghasemi, H.R., Collins, A.L., 2020c. A new integrated data mining model to map spatial variation in the susceptibility of land to act as a source of aeolian dust. Environ. Sci. Pollut. Control Ser. 27, 42022–42039.

Gholami, H., Mohammadifar, A., Golzari, S., Kaskaoutis, D.G., Collins, A.L., 2021. Using the Boruta algorithm and deep learning models for mapping land susceptibility to atmospheric dust emissions in Iran. Aeolian Research 50, 100682.

Ghorbanian, A., Kakooei, M., Amani, M., Mahdavi, S., Mohammadzadeh, A., Hasanlou, M., 2020. Improved land cover map of Iran using Sentinel imagery within Google Earth Engine and a novel automatic workflow for land cover classification using migrated training samples. ISPRS J. Photogrammetry Remote Sens. 167, 276–288.

Gillette, D.A., 1999. A qualitative geophysical explanation for''hot spot''dust emitting source regions. Contrib. Atmos. Phys. 72.

Goudarzi, G., Daryanoosh, S.M., Godini, H., Hopke, P.K., Sicard, P., De Marco, A., et al., 2017. Health risk assessment of exposure to the Middle-Eastern Dust storms in the Iranian megacity of Kermanshah. Publ. Health 148, 109–116.

Hamzeh, N.H., Kaskaoutis, D.G., Rashki, A., Mohammadpour, K., 2021. Long-term variability of dust events in southwestern Iran and its relationship with the drought. Atmosphere 12 (10), 1350.

Houssein, E.H., Hosney, M.E., Mohamed, W.M., Ali, A.A., Younis, E.M., 2023. Fuzzy-based hunger games search algorithm for global optimization and feature selection using medical data. Neural Comput. Appl. 35 (7), 5251–5275.

Jafari, R., Amiri, M., Asgari, F., Tarkesh, M., 2022. Dust source susceptibility mapping based on remote sensing and machine learning techniques. Ecol. Inf. 72, 101872.

Jain, M., Saihjpal, V., Singh, N., Singh, S.B., 2022. An overview of variants and advancements of PSO algorithm. Appl. Sci. 12 (17), 8392.

Jiao, P., Wang, J., Chen, X., Ruan, J., Ye, X., Alavi, A.H., 2021. Next-generation remote sensing and prediction of sand and dust storms: state-of-the-art and future trends. Int. J. Rem. Sens. 42 (14), 5277–5316.

Jin, Y., O'Connor, D., Ok, Y.S., Tsang, D.C., Liu, A., Hou, D., 2019. Assessment of sources of heavy metals in soil and dust at children's playgrounds in Beijing using GIS and multivariate statistical analysis. Environ. Int. 124, 320–328.

Joseph, L.P., Joseph, E.A., Prasad, R., 2022. Explainable diabetes classification using hybrid Bayesian-optimized TabNet architecture. Comput. Biol. Med. 151, 106178.

Juneja, M., Nagar, S.K., 2016. Particle swarm optimization algorithm and its parameters: a review. In: 2016 International Conference on Control, Computing, Communication and Materials (ICCCCM). IEEE, pp. 1–5. October.

Kameyama, K., 2009. Particle swarm optimization-a survey. IEICE Trans. Info Syst. 92 (7), 1354–1361.

Kavouras, I.G., Etyemezian, V., Xu, J., DuBois, D.W., Green, M., Pitchford, M., 2007. Assessment of the local windblown component of dust in the western United States. J. Geophys. Res. Atmos. 112 (D8).

Kedia, S., Kumar, R., Islam, S., Sathe, Y., Kaginalkar, A., 2018. Radiative impact of a heavy dust storm over India and surrounding oceanic regions. Atmos. Environ. 185, 109–120.

Kellogg, C.A., Griffin, D.W., 2006. Aerobiology and the global transport of desert dust. Trends Ecol. Evol. 21 (11), 638–644.

Khan, R.K., Strand, M.A., 2018. Road dust and its effect on human health: a literature review. Epidemiology and health 40.

Kulkarni, M.N.K., Patekar, M.S., Bhoskar, M.T., Kulkarni, M.O., Kakandikar, G.M., Nandedkar, V.M., 2015. Particle swarm optimization applications to mechanical engineering-A review. Mater. Today: Proc. 2 (4–5), 2631–2639.
Lee, J.H., Sameen, M.I., Pradhan, B., Park, H.J., 2018. Modeling landslide susceptibility in data-scarce environments using optimized data mining and statistical methods. Geomorphology 303, 284–298.
Leung, D.M., Kok, J.F., Li, L., Okin, G.S., Prigent, C., Klose, M., et al., 2022. A new process-based and scale-respecting desert dust emission scheme for global climate models–Part I: description and evaluation against inverse modeling emissions. Atmos. Chem. Phys. Discuss. 1–58.
Li, X., Luk, K.M., 2019. The grey wolf optimizer and its applications in electromagnetics. IEEE Trans. Antenn. Propag. 68 (3), 2186–2197.
Liu, L., Cai, G., Zhang, J., Liu, X., Liu, K., 2020. Evaluation of engineering properties and environmental effect of recycled waste tire-sand/soil in geotechnical engineering: a compressive review. Renew. Sustain. Energy Rev. 126, 109831.
Ma, B.J., Liu, S., Heidari, A.A., 2022. Multi-strategy ensemble binary hunger games search for feature selection. Knowl. Base Syst. 248, 108787.
Mahajan, S., Abualigah, L., Pandit, A.K., 2022. Hybrid arithmetic optimization algorithm with hunger games search for global optimization. Multimed. Tool. Appl. 81 (20), 28755–28778.
Mallick, J., Alashker, Y., Mohammad, S.A.D., Ahmed, M., Hasan, M.A., 2014. Risk assessment of soil erosion in semi-arid mountainous watershed in Saudi Arabia by RUSLE model coupled with remote sensing and GIS. Geocarto Int. 29 (8), 915–940.
Mani, M., Pillai, R., 2010. Impact of dust on solar photovoltaic (PV) performance: research status, challenges and recommendations. Renew. Sustain. Energy Rev. 14 (9), 3124–3131.
Manisalidis, I., Stavropoulou, E., Stavropoulos, A., Bezirtzoglou, E., 2020. Environmental and health impacts of air pollution: a review. Front. Public Health 14.
Masroor, M., Razavi-Termeh, S.V., Rahaman, M.H., Choudhari, P., Kulimushi, L.C., Sajjad, H., 2023. Adaptive neuro fuzzy inference system (ANFIS) machine learning algorithm for assessing environmental and socio-economic vulnerability to drought: a study in Godavari middle sub-basin, India. Stoch. Environ. Res. Risk Assess. 37 (1), 233–259.
McDonnell, K., Murphy, F., Sheehan, B., Masello, L., Castignani, G., 2023. Deep learning in insurance: accuracy and model interpretability using TabNet. Expert Syst. Appl. 119543.
Mehravar, S., Razavi-Termeh, S.V., Moghimi, A., Ranjgar, B., Foroughnia, F., Amani, M., 2023. Flood susceptibility mapping using multi-temporal SAR imagery and novel integration of nature-inspired algorithms into support vector regression. J. Hydrol. 129100.
Murdoch, W.J., Singh, C., Kumbier, K., Abbasi-Asl, R., Yu, B., 2019. Definitions, methods, and applications in interpretable machine learning. Proc. Natl. Acad. Sci. USA 116 (44), 22071–22080.
Muthukumar, P., Nagrecha, K., Comer, D., Calvert, C.F., Amini, N., Holm, J., Pourhomayoun, M., 2022. PM2. 5 air pollution prediction through deep learning using multisource meteorological, wildfire, and heat data. Atmosphere 13 (5), 822.
Nadimi-Shahraki, M.H., Taghian, S., Mirjalili, S., 2021. An improved grey wolf optimizer for solving engineering problems. Expert Syst. Appl. 166, 113917.
Namdari, S., Zghair Alnasrawi, A.I., Ghorbanzadeh, O., Sorooshian, A., Kamran, K.V., Ghamisi, P., 2022. Time series of remote sensing data for interaction analysis of the vegetation coverage and dust activity in the Middle East. Rem. Sens. 14 (13), 2963.
Ogunwole, J.O., Chaudhary, D.R., Ghosh, A., Daudu, C.K., Chikara, J., Patolia, J.S., 2008. Contribution of Jatropha curcas to soil quality improvement in a degraded Indian entisol. Acta Agric. Scand. Sect. B Soil Plant Sci 58 (3), 245–251.
Onwunalu, J.E., Durlofsky, L.J., 2010. Application of a particle swarm optimization algorithm for determining optimum well location and type. Comput. Geosci. 14, 183–198.
Parween, S., Siddique, N.A., Diganta, M.T.M., Olbert, A.I., Uddin, M.G., 2022. Assessment of urban river water quality using modified NSF water quality index model at Siliguri city, West Bengal, India. Environmental and Sustainability Indicators 16, 100202.
Pourhashemi, S., Asadi, M.A.Z., Boroughani, M., Azadi, H., 2022. Mapping of dust source susceptibility by remote sensing and machine learning techniques (case study: Iran-Iraq border). Environ. Sci. Pollut. Control Ser. 1–15.
Prokof'eva, T.V., Kiryushin, A.V., Shishkov, V.A., Ivannikov, F.A., 2017. The importance of dust material in urban soil formation: the experience on study of two young Technosols on dust depositions. J. Soils Sediments 17, 515–524.
Prospero, J.M., Ginoux, P., Torres, O., Nicholson, S.E., Gill, T.E., 2002. Environmental characterization of global sources of atmospheric soil dust identified with the Nimbus 7 Total Ozone Mapping Spectrometer (TOMS) absorbing aerosol product. Rev. Geophys. 40 (1), 2-1.
Rahi, G., Bahreini, F., Khosroshahi, M., Biabani, L., 2022. The effect of drought on dust storm frequency (case study: Bushehr province). Journal of Water and Soil Conservation 29 (1), 31–51.
Rashki, A., Kaskaoutis, D.G., Sepehr, A., 2018. Statistical evaluation of the dust events at selected stations in southwest Asia: from the caspian sea to the arabian sea. Catena 165, 590–603.
Rashki, A., Middleton, N.J., Goudie, A.S., 2021. Dust storms in Iran–Distribution, causes, frequencies and impacts. Aeolian Research 48, 100655.
Razavi-Termeh, S.V., Sadeghi-Niaraki, A., Choi, S.M., 2021. Spatial modeling of asthma-prone areas using remote sensing and ensemble machine learning algorithms. Rem. Sens. 13 (16), 3222.
Razavi-Termeh, S.V., Sadeghi-Niaraki, A., Seo, M., Choi, S.M., 2023. Application of genetic algorithm in optimization parallel ensemble-based machine learning algorithms to flood susceptibility mapping using radar satellite imagery. Sci. Total Environ. 873, 162285.
Reynolds, R., Belnap, J., Reheis, M., Lamothe, P., Luiszer, F., 2001. Aeolian dust in Colorado Plateau soils: nutrient inputs and recent change in source. Proc. Natl. Acad. Sci. USA 98 (13), 7123–7127.
Rezaei, M., Riksen, M.J., Sirjani, E., Sameni, A., Geissen, V., 2019. Wind erosion as a driver for transport of light density microplastics. Sci. Total Environ. 669, 273–281.
Rouzrokh, P., Khosravi, B., Faghani, S., Moassefi, M., Vera Garcia, D.V., Singh, Y., et al., 2022. Mitigating bias in radiology machine learning: 1. Data handling. Radiology: Artif. Intell. 4 (5), e210290.
Sahu, A., Mishra, D.P., 2023. Effects of intrinsic properties, particle size, bulk density, and specific gravity on thermal properties of coal dusts. Environ. Sci. Pollut. Control Ser. 1–17.
Shabanpour, N., Razavi-Termeh, S.V., Sadeghi-Niaraki, A., Choi, S.M., Abuhmed, T., 2022. Integration of machine learning algorithms and GIS-based approaches to cutaneous leishmaniasis prevalence risk mapping. Int. J. Appl. Earth Obs. Geoinf. 112, 102854.
Shah, C., Du, Q., Xu, Y., 2022. Enhanced TabNet: attentive interpretable tabular learning for hyperspectral image classification. Rem. Sens. 14 (3), 716.
Shahin, I., Alomari, O.A., Nassif, A.B., Afyouni, I., Hashem, I.A., Elnagar, A., 2023. An efficient feature selection method for Arabic and English speech emotion recognition using Grey Wolf Optimizer. Appl. Acoust. 205, 109279.
Si, C., Chen, W., Wang, W., Wang, L., Tan, T., 2019. An attention enhanced graph convolutional lstm network for skeleton-based action recognition. In *Proceedings of the IEEE/CVF Conference on Computer Vision and Pattern Recognition*, pp. 1227–1236.
Sowden, M., Mueller, U., Blake, D., 2018. Review of surface particulate monitoring of dust events using geostationary satellite remote sensing. Atmos. Environ. 183, 154–164.
Sun, T., Che, H., Qi, B., Wang, Y., Dong, Y., Xia, X., et al., 2018. Aerosol optical characteristics and their vertical distributions under enhanced haze pollution events: effect of the regional transport of different aerosol types over eastern China. Atmos. Chem. Phys. 18 (4), 2949–2971.
Tam, W.W., Wong, T.W., Wong, A.H., Hui, D.S., 2012. Effect of dust storm events on daily emergency admissions for respiratory diseases. Respirology 17 (1), 143–148.
Tehrany, M.S., Pradhan, B., Jebur, M.N., 2014. Flood susceptibility mapping using a novel ensemble weights-of-evidence and support vector machine models in GIS. J. Hydrol. 512, 332–343.
Tikhamarine, Y., Souag-Gamane, D., Ahmed, A.N., Kisi, O., El-Shafie, A., 2020. Improving artificial intelligence models accuracy for monthly streamflow forecasting using grey Wolf optimization (GWO) algorithm. J. Hydrol. 582, 124435.
Tong, D.Q., Gill, T.E., Sprigg, W.A., Van Pelt, R.S., Baklanov, A.A., Barker, B.M., et al., 2021. Health and safety effects of airborne soil dust in the Americas and beyond. Rev. Geophys., e2021RG000763
Uddin, M.G., Nash, S., Diganta, M.T.M., Rahman, A., Olbert, A.I., 2022. Robust machine learning algorithms for predicting coastal water quality index. J. Environ. Manag. 321, 115923.
Uddin, M.G., Nash, S., Rahman, A., Olbert, A.I., 2023a. Performance analysis of the water quality index model for predicting water state using machine learning techniques. Process Saf. Environ. Protect. 169, 808–828.
Uddin, M.G., Nash, S., Rahman, A., Olbert, A.I., 2023b. Assessing optimization techniques for improving water quality model. J. Clean. Prod. 385, 135671.
Uddin, M.G., Nash, S., Rahman, A., Olbert, A.I., 2023c. Performance analysis of the water quality index model for predicting water state using machine learning techniques. Process Saf. Environ. Protect. 169, 808–828.
Von Holdt, J.R.C., Eckardt, F.D., Baddock, M.C., Wiggs, G.F., 2019. Assessing landscape dust emission potential using combined ground-based measurements and remote sensing data. J. Geophys. Res.: Earth Surf. 124 (5), 1080–1098.
Von Holdt, J.R., Eckardt, F.D., Wiggs, G.F.S., 2017. Landsat identifies aeolian dust emission dynamics at the landform scale. Rem. Sens. Environ. 198, 229–243.
Wang, C., Wang, J., Naudiyal, N., Wu, N., Cui, X., Wei, Y., Chen, Q., 2021. Multiple effects of topographic factors on Spatio-temporal variations of vegetation patterns in the three parallel rivers region, Southeast Qinghai-Tibet Plateau. Rem. Sens. 14 (1), 151.
Yan, J., Xu, T., Yu, Y., Xu, H., 2021. Rainfall forecast model based on the tabnet model. Water 13 (9), 1272.
Yang, H., Zhang, X., Zhao, F., Wang, J.A., Shi, P., Liu, L., 2015. Mapping sand-dust storm risk of the world. World Atlas of Natural Disaster Risk, pp. 115–150.
Yang, Y., Chen, H., Heidari, A.A., Gandomi, A.H., 2021. Hunger games search: visions, conception, implementation, deep analysis, perspectives, and towards performance shifts. Expert Syst. Appl. 177, 114864.
Zeinali, B., Asghari, S., 2016. Mapping and monitoring of dust storms in Iran by fuzzy clustering and remote sensing techniques. Arabian J. Geosci. 9, 1–10.
Zucca, C., Middleton, N., Kang, U., Liniger, H., 2021. Shrinking water bodies as hotspots of sand and dust storms: the role of land degradation and sustainable soil and water management. Catena 207, 105669.